Monsoon low pressure system like variability in an idealized moist model Spencer K. Clark* Program in Atmospheric and Oceanic Sciences, Princeton University, Princeton, New Jersey Yi Ming Geophysical Fluid Dynamics Laboratory/NOAA, Princeton, New Jersey Ángel F. Adames Department of Climate and Space Science and Engineering, University of Michigan, Ann Arbor, Michigan *Corresponding author address: Program in Atmospheric and Oceanic Sciences, Princeton University, 219 Sayre Hall 300 Forrestal Road, Princeton, NJ, USA. E-mail: skclark@princeton.edu Generated using v4.3.2 of the AMS LATEX template

Early Online Release: This preliminary version has been accepted for publication in *Journal of Climate*, may be fully cited, and has been assigned DOI 10.1175/JCLI-D-19-0289.1. The final

typeset copyedited article will replace the EOR at the above DOI when it is published.

© 2019 American Meteorological Society

ABSTRACT

In this paper, it is shown that westward-propagating monsoon-low-pressuresystem-like disturbances in the South Asian monsoon region can be simulated
in an idealized moist general circulation model through the addition of a simplified parameterization of land. Land is parameterized as having one-tenth
the heat capacity of the surrounding slab ocean, with evaporation limited by
a bucket hydrology model. In this model, the prominent topography of the
Tibetan Plateau does not appear to be necessary for these storm systems to
form or propagate; therefore focus is placed on the simulation with land but
no topography.

The properties of the simulated storms are elucidated using regression analysis and compared to results from composites of storms from comprehensive
GCMs in prior literature and reanalysis. The storms share a similar vertical

ysis and compared to results from composites of storms from comprehensive
GCMs in prior literature and reanalysis. The storms share a similar vertical
profile in anomalous Ertel potential vorticity to those in reanalysis. Propagation, however, does not seem to be strongly dictated by beta-drift. Rather,
it seems to be more closely consistent with linear moisture vortex instability
theory, with the exception of the importance of the vertical advection term
in the Ertel potential vorticity budget toward the growth and maintenance of
disturbances. The results presented here suggest that a simplified GCM configuration might be able to be used to gain a clearer understanding of the
sensitivity of monsoon low pressure systems to changes in the mean state cli-

mate.

3 1. Introduction

South Asia has a monsoonal climate. It receives 50 % to 70 % of its annual precipitation during the months of June, July, and August (Neelin 2007). During these months, moist static energy is abundant, fueling monsoon low pressure systems (MLPSs) which originate in the Bay of Bengal and propagate westward against the direction of the prevailing mean low-level winds, across India 37 at speeds of around 4 m s⁻¹ (Adames and Ming 2018a). Studies in recent years have attributed between 50% and 60% of monsoon season rainfall in central India to these lows (Hurley and Boos 2015; Praveen et al. 2015; Hunt and Fletcher 2019). For that reason, understanding what influences 40 the propagation and structure of these transient phenomena is important for understanding what controls precipitation during the summer in South Asia. The growth, propagation, and structure of these low pressure systems has been an area of re-43 search for several decades, dating back to Godbole (1977) and references therein. In recent years effort has been made by multiple independent research groups to compile detailed track information for monsoonal disturbances (Hurley and Boos 2015; Hunt et al. 2016a). This effort has led to new insights resulting from rigorous analysis of the composite properties of these storms (Hurley and Boos 2015; Boos et al. 2015; Ditchek et al. 2016; Hunt et al. 2016a,b; Cohen and Boos 2016; Sandeep et al. 2018). In particular, early theoretical attempts to explain the growth and propagation of monsoon depressions in terms of barotropic (Shukla 1977; Lindzen et al. 1983), baroclinic (Mishra and Salvekar 1980; Mak 1983; Moorthi and Arakawa 1985), or combined barotropic-51 baroclinic (Krishnamurti et al. 1976; Shukla 1978) instability mechanisms have recently been challenged by a number of alternative ideas.

- An example where these early ideas were challenged is the study by Cohen and Boos (2016).
- They investigated composites of observed monsoon depressions in reanalysis and compared them

with the canonical example of moist baroclinic instability: diabatic Rossby waves in the midlatitudes. They found that in monsoon depressions, anomalies in Ertel potential vorticity do not 57 tilt against the mean vertical wind shear as they do in diabatic Rossby waves, which they argue is 58 evidence against moist baroclinic instability operating as a mechanism in fueling the growth of the disturbances. In their paper Cohen and Boos (2016) also invoke results from Krishnamurti et al. (2013) to argue that barotropic instability plays a minor, if any, role in the development of MLPSs. 61 In Krishnamurti et al. (2013) it was found that kinetic energy from the eddies in observed MLPSs was transferred to the mean zonal flow, counter to what occurs in barotropically unstable flows. In the last five years, four, possibly overlapping, alternative explanations for monsoonal dis-64 turbance propagation have been proposed. The first is that monsoon depressions might be better described as tropical-cyclone-like features propagating via adiabatic beta drift (Boos et al. 2015), though perhaps without as strong a dependence on surface fluxes, which have been shown to be 67 important for tropical cyclones (Muller and Romps 2018). Another possible explanation, proposed in Hunt and Parker (2016), is that the Himalayan mountains may act as a rigid northern meridional boundary in the lower troposphere, leading to westward propagation of a cyclonic vortex to the 70 south via an effective mirror-image vortex. Adames and Ming (2018b) develop a linear theory 71 for monsoonal disturbances within a mid-latitude moisture-mode like framework, where the instability depends necessarily on the inclusion of a prognostic moisture equation. Finally, Diaz and 73 Boos (2019) revisit the potential influence of barotropic instability, and find that in the absence of convective heating, growing disturbances fueled by barotropic instability could be possible with a zonally-uniform basic state; however these disturbances did not grow at rates consistent with observed storms, motivating future study in a moist framework. These theories are still young, and their utility for explaining the properties of monsoonal disturbances and their potential sensitivity

- to changes in the mean state, e.g. induced by increasing greenhouse gas concentrations, has yet to be extensively investigated.
- The complications of the real world, however, make monsoonal disturbances difficult to study.

 For instance many comprehensive general circulation models used in the fifth phase of the Coupled Model Intercomparison Project (CMIP5) (Taylor et al. 2012) struggle to obtain a realistic distribution of climatological mean June, July, August, and September (JJAS) precipitation rate in the South Asian monsoon region (see the supplement of Sandeep et al. 2018). In addition, several models run under the Atmospheric Model Intercomparison Project (AMIP) protocol (Gates 1992) simulate unrealistic patterns of synoptic activity index (SAI) (also see the supplement of Sandeep et al. 2018), a metric that quantifies an intensity-weighted frequency of MLPS days per season at each location (Ajayamohan et al. 2010). To some extent these errors are attributed to the coarse horizontal resolution of these models; indeed studies have shown that models run with higher resolution such as the UK Met Office's Unified Model or the Geophysical Fluid Dynamics Laboratory's (GFDL's) HiRAM demonstrate increased skill in simulating MLPSs (Hunt and
- Despite sometimes having errors in the exact location of storms, however, some coarseresolution General Circulation Models (GCMs) (such as GFDL's AM4) have been shown to have
 the ability to reasonably simulate their general frequency statistics and structure (Adames and
 Ming 2018a), indicating that exact-realism of precipitation location and mean winds is not necessarily required for studying the structure and propagation of these dynamical phenomena. It
 prompts the question of whether a simpler model, lower in the complexity hierarchy, could capture the essence of MLPSs. By a simpler model, we mean one somewhere in between an idealized
 aquaplanet GCM (like Frierson et al. 2006) and a comprehensive GCM (complete with intricate

Turner 2017; Sandeep et al. 2018).

93

instance, found abundant westward-propagating cyclonic vorticity anomalies, akin to MLPSs, in a simulation using a very coarse horizontal resolution GCM (T21 spectral truncation) and heavily simplified lower boundary conditions. It is worth revisiting these disturbances in a similar setup in light of recent developments (e.g. Boos et al. 2015; Cohen and Boos 2016; Hunt and Parker 2016; Adames and Ming 2018b,a; Diaz and Boos 2019).

In this study we start from a version of Frierson et al. (2006)'s idealized moist model coupled to a full radiative transfer code (Clark et al. 2018), and build up in complexity to attain an environment capable of supporting MLPS-like disturbances. We use this setup, coupled with detailed analysis of the composite anomalous budgets of Ertel potential vorticity, relative vorticity, column internal energy, and column moisture, to discuss the potential applicability of the theories for MLPS propagation described above, and touch on the importance of various boundary conditions, like topography, in the realism of the disturbances simulated.

5 2. Methods

116 a. Model description

The modeling setup we use to simulate MLPSs is heavily idealized. Our starting point is the GFDL idealized moist model as configured in Clark et al. (2018). This global model was first introduced in Frierson et al. (2006, 2007), where it consisted of a spectral dynamical core, with simplified moist physics, boundary layer, and radiation parameterizations. It has since been modified to include a simplified Betts-Miller moist convection scheme (Frierson 2007b)¹, alterations to

¹An important parameter in this convection scheme is the relaxation time; we use a relaxation time of 2 h, which is the typical default value used by other studies (e.g. Frierson 2007b; O'Gorman and Schneider 2008; Geen et al. 2017). While it has been shown that aspects of the climate can be sensitive to this parameter choice (e.g. Frierson 2007a; Clark et al. 2018), we find qualitatively similar results in an experiment with a larger convective relaxation time (12 h; not shown), which has been suggested by Bretherton et al. (2004) to potentially be a more appropriate convective relaxation time scale for convection parameterizations of the type used in this model.

tive transfer, rather than the original gray radiative transfer scheme (Clark et al. 2018). While the full radiative transfer scheme interacts with the active water vapor tracer in the model, there is no parameterization of cloud condensate, and therefore no cloud radiative effects or feedbacks. Slab ocean aquaplanet configurations similar to this, i.e. full radiative transfer with simplified moist physics, have been used before, e.g. in Merlis et al. (2012a,b), Jucker and Gerber (2017), and Vallis et al. (2018).

In this study, we examine MLPSs in the South Asia region. Due to the annual cycle in solar in-129 solation, these primarily occur in the boreal summer months of June, July, August, and September, 130 but can also occur during other parts of the year (Hurley and Boos 2015). To capture this seasonal 131 variation in climate, we run all of our simulations with Earth's current approximate obliquity 132 and eccentricity parameters, 23.439° and 0.01671 respectively. In addition we introduce a crude 133 parameterization of land. In prior studies, land has been added to variants of this model with vary-134 ing degrees of complexity depending on the application, typically involving modification of some combination of the heat capacity, evaporation parameterization, surface roughness, surface albedo, 136 and surface height over the land portion of the domain (e.g. Byrne and O'Gorman 2012; Merlis 137 et al. 2012b; Maroon et al. 2016; Maroon and Frierson 2016; Voigt et al. 2016; Geen et al. 2017; Vallis et al. 2018; Zhou and Xie 2018). In other models, simplified land has been added in similar 139 ways (e.g. Xie and Saiki 1999; Becker and Stevens 2014; Cronin et al. 2015). As a starting point 140 in our model we choose to distinguish land from the default lower boundary, a slab ocean, in only two ways: its heat capacity, and its treatment of evaporation. 142

The land setup maintains the slab ocean model across the entire lower boundary; however, over land grid cells we use a shallower mixed layer depth, which controls the heat capacity, and scale the potential evaporation rate as predicted by the bulk formula over a saturated surface by a fraction

determined using a simple bucket hydrology model, the same as described in Vallis et al. (2018), which is similar to that in Byrne and O'Gorman (2012) or Zhou and Xie (2018), which dates back 147 to Manabe (1969). The mixed layer depths over land and ocean are the same as those used in 148 experiments in Geen et al. (2017), 2 m over land and 20 m over ocean, and the bucket hydrology model parameters are the same as those described in Vallis et al. (2018), a bucket depth of 150 mm 150 and a bucket saturation fraction of 0.75. We use a surface albedo of 0.26 over land and ocean. The 151 global mean surface albedo is greater than it might be in a comprehensive GCM as to increase the 152 planetary albedo in the absence of clouds (Frierson et al. 2006). Finally, we prescribe zero heat 153 flux from the ocean to the atmosphere, meaning, as a simplification, we assume the ocean does not 154 facilitate any horizontal energy transport. We assume the same for land regions. 155

In principle one could tune the mixed layer depths, surface albedo, bucket hydrology scheme 156 parameters, and prescribed ocean heat fluxes [e.g. following the procedure outlined in Vallis et al. 157 (2018)] to produce a mean state climate as close as possible to that in observations. However, to 158 maintain a connection to simpler configurations we elect to use the setup described above, which 159 produces a mean state climate that resembles that in observations, but is not an exact match (e.g. 160 it does not contain a significant Western Pacific Warm Pool signature, or east-west asymmetry in 161 ocean basin SST due to warm western boundary currents). For a comparison of the mean state in 162 our simulation to that in observations, see Figure S1, which compares the global pattern in JJAS 163 mean precipitation rate and surface temperature in our idealized simulation to that in Tropical 164 Rainfall Measurement Mission (TRMM) observations (Huffman et al. 2007) and ERA-Interim reanalysis (Dee et al. 2011). 166

With regard to atmospheric composition, we use approximately present-day concentrations of the well-mixed greenhouse gases ($CO_2 = 369.4 \text{ ppm}$, $CH_4 = 1.821 \text{ ppm}$), and prescribe a

hemispherically-symmetric pattern of ozone, based on the pattern used in the Aqua-Planet Model Intercomparison Project (Blackburn et al. 2013).

Similar to Geen et al. (2017), to improve the numerical stability of the dynamical core in the upper levels of the model, we add a Rayleigh damping tendency to the horizontal winds. The Rayleigh damping coefficient we use decreases faster than linearly from a value near 0.33 d⁻¹ at the top of the model to near zero near the surface, following the vertical profile defined in Equations 13.89 and 13.90 in Jablonowski and Williamson (2011), which were first used in Boville (1986). This Rayleigh damping profile was used for several years in the European Centre for Medium-Range Weather Forecasts (ECMWF) Integrated Forecast System (IFS) model (Jablonowski and Williamson 2011).

179 b. Experiments

In this study we focus on a simulation with "land" as described in Section 2.a, with realistic 180 contintental geometry, but flat topography. We run the model for 20 years, starting from spatiallyuniform initial conditions (constant initial temperature and specific humidity), storing 6-hourly 182 mean values of the relevant diagnostics. After the first 10 years, the model approximately reaches 183 equilibrium, here defined as the moment at which the annual global mean net top of atmosphere radiative flux begins to hold steady at near zero. Accordingly, we use the final ten years of each 185 simulation for analysis. The model is configured with 40 unevenly-spaced vertical sigma levels, 186 with approximately three levels within the planetary boundary layer, and extends to the top of the atmosphere, with a top-level interface pressure of 0 hPa. In the horizontal, we run the model at 188 T42 spectral resolution, which corresponds to approximately $2.8^{\circ} \times 2.8^{\circ}$ horizontal resolution in 189 grid space.

As part of this study, we ran two other simulations flanking the simulation described above in 191 terms of the complexity of the lower boundary, though we do not show their results. On the simpler 192 side, we ran an aquaplanet case with a uniform slab ocean mixed layer depth of 20 m, while on the 193 more complex side, we ran a case with land and realistic topography, spectrally regularized as in 194 Lindberg and Broccoli (1996). The aquaplanet case produced an annual cycle in precipitation significantly lagged from that on Earth's, with monthly mean precipitation rates maximizing during 196 September and October at the latitudes of the South Asian monsoon region. It also lacked a real-197 istic polewardly-increasing meridional temperature gradient and attendent easterly vertical wind shear². On the other hand, the case with realistic topography produced MLPSs, but despite regu-199 larization, suffered from severe spectral ringing in the mean precipitation field near the Himalayas, 200 compromising the quality of the climate relative to the flat topography case. Therefore the config-201 uration with land and flat topography happened to be the best configuration of this model we tested 202 for studying South Asian MLPSs. It is possible that one could obtain MLPS-like disturbances in a 203 simulation with further idealized contintental geometry and surface hydrology. However we leave such experimentation to future work and choose to focus on our realistic contintental geometry, 205 flat topography simulation, which provides an important link between MLPSs in comprehensive 206 GCMs and those in more idealized frameworks.

²One could potentially produce a more realistic meridional temperature gradient, and potentially MLPSs, in the aquaplanet configuration of this model by removing the seasonal cycle in solar insolation and adding a forcing to induce a warm pool at the latitudes of the South Asian monsoon region, e.g. centered at around 15°N. For instance Ajayamohan et al. (2014) find westward propagating Rossby-wave-like disturbances in such a setup; however, in this study we opt to allow the natural interaction between the seasonal cycle and land-ocean contrast in heat capacity to produce such a local temperature maximum in the region.

208 c. Analysis techniques

To analyze the structure of MLPSs in our model, we employ frequency-wavenumber spectral analysis, compute lag regression patterns, and tracer budgets. Frequency-wavenumber spectral 210 analysis allows us to identify the frequencies and wavenumbers of the zonally-propagating waves 211 that are most prevalent; this type of analysis is commonly used in studying equatorial waves (e.g. 212 Wheeler and Kiladis 1999; Hendon and Wheeler 2008), though here we apply the technique in 213 the latitudes of the South Asian monsoon region. Lag regression patterns allow us to determine 214 the spatial structure of variable anomalies projected onto a MLPS index. Tracer budget analysis 215 allows us to determine the leading terms governing the evolution of MLPSs in our model. We 216 approximately follow the methods described in Adames and Ming (2018a). Here we will explain 217 the details of these techniques which we will employ later.

219 1) SPECTRAL ANALYSIS

To compute frequency-wavenumber power spectra, we start with 6-hourly resolution model out-220 put of the precipitation rate. We then subset this dataset in time such that it only includes datapoints 221 for the months of June, July, August, and September. From this timeseries, we construct a set of 222 60-day segments, which overlap by 30 days, generating a four-dimensional dataset, with dimen-223 sions time, longitude, segment, and latitude; it follows that the segment dimension has length 242. We apply a Hanning window over the time dimension, tapering the endpoints of the segments 225 toward zero to minimize spectral leakage (Welch 1967); in addition, we apply a Hanning win-226 dow over 50°E to 130°E to taper data to zero outside our longitudinal region of interest. After this preparation, we compute a fast Fourier transform (FFT) in longitude and time, and compute 228 the power as the square of the magnitude of the complex Fourier coefficients. To construct a 229 two-dimensional frequency-wavenumber diagram, we average the power over the segments and

between latitudes bounding the region of interest for the particular dataset, which correspond roughly to the latitudinal bounds of the South Asian monsoon region, and then compare it to a reference red frequency spectrum. We define the region of interest for a particular dataset as $\pm 5^{\circ}$ from the latitude of maximum mean JJAS precipitation rate³ along the 80°E longitude band. We compute the red spectrum as in Masunaga et al. (2006), normalizing such that the sum of the power in non-zero frequencies matches that in the power spectrum of the precipitation rate.

To compare the power in the signal to that in the reference red spectrum, we compute what is referred to as the "signal strength" (S) by determining the ratio of the difference between the power spectrum (P) and red spectrum (R) to the power spectrum itself:

$$S = \frac{P - R}{P} = \frac{P/R - 1}{P/R}.\tag{1}$$

Statistical significance is determined by computing a critical value of a chi-squared-statistic at the 99% significance level, which is the ratio of two variances scaled by the degrees of freedom (n) minus one, e.g. $\chi^2 = \frac{P(n-1)}{R}$. The number of degrees of freedom used in computing the critical chi-squared value is calculated as in Hendon and Wheeler (2008) and Adames and Ming (2018b); it is equal to 2 (amplitude and phase) x 10 (number of years) x 122 (number of days in JJAS per year) / 60 (days per segment) \approx 40. At the 99% level, this results in a critical χ^2 -value of 62.4, indicating that if the power of the signal is 1.6 times that of the red spectrum then there is a 1% chance the signal emerged out of red noise. In terms of the signal strength in Equation 1, this means in order for the signal to be statistically significant at the 99% level, the signal strength must be greater than or equal to approximately 0.38:

$$\frac{\chi_{\text{critical}}^2}{n-1} = \left(\frac{P}{R}\right)_{\text{critical}} = 1.6 \implies S_{\text{critical}} = 0.38.$$
 (2)

³Hurley and Boos (2015) note that MLPS activity is strongest slightly poleward of this maximum in most monsoon regions; however we claim that as a first approximation this is a reasonable method of defining the central latitude of our region of interest.

50 2) LAG REGRESSION ANALYSIS

To compute lag regression patterns we follow the methods of Adames and Wallace (2014) and Adames and Ming (2018a). This requires computing an index, which measures the intensity of 252 MLPS activity. Adames and Ming (2018a) do this by spectrally filtering the precipitation rate to 253 include wave activity from only MLPS-like modes (zonal wavenumbers, k, between -25 and -3254 and frequencies greater than 0.067 d⁻¹), then averaging over the spatial region of interest, here 255 defined as $\pm 5^{\circ}$ latitude from the latitude of maximum JJAS mean precipitation rate, between 256 75°E and 85°E in longitude; this results in a one-dimensional index over time, which is then 257 standardized such that it has a mean of zero and a standard deviation of one, yielding a vector \mathbf{P}^T . 258 Here k is the non-dimensional zonal wavenumber, which can be related to a dimensional zonal 259 wavenumber \tilde{k} via $k = \tilde{k}a\cos\phi$, where a is the radius of the Earth and ϕ is latitude. The spectral 260 filtering is achieved by performing standard Fourier transforms in time and longitude of the raw 261 precipitation rate timeseries, zeroing out all coefficients outside of the rectangular spectral region 262 specified above, and computing an inverse Fourier transform back to time and longitude space. 263 With an index in hand, we can then regress any variable against it. Borrowing notation from Adames and Wallace (2014) this looks like: 265

$$\mathbf{D} = \frac{\mathbf{S}\mathbf{P}^T}{N}.\tag{3}$$

Here **S** is a two-dimensional matrix with each row representing the time series of a variable at a given gridcell. To ensure that we are capturing the anomalies associated with high-frequency, i.e. storm-timescale, variablity, we spectrally filter all quantities we regress such that they contain frequencies of only $0.067 \, d^{-1}$ and above; this approach is analogous to the approach used in Kim et al. (2013), who filtered the meridional advection term of the column-integrated MSE budget to periods between 20 d to 100 d before regressing, to isolate MJO-related anomalies. **P** is the

standardized index at each time, i.e. it is a single row vector; N is the number of values in the index; and \mathbf{D} is the computed regression pattern. \mathbf{D} contains a time-independent spatial pattern of anomalies with the same spatial dimensions as the input variable. Lag regressions can be computed by shifting the index forward or backward in time and applying the same procedure, noting that this reduces the number of overlapping elements between the index and variable, i.e. it slightly changes N. This allows us to construct a picture of what the conditions look like before, during, and after a monsoon low pressure system event occurs.

To smooth out regression patterns, particularly in the context of the tracer budgets, we apply a regression-compositing technique similar to the one employed in Adames and Ming (2018a). This entails computing regression patterns for index regions shifted -2, -1, 0, 1, or 2 grid cells away in longitude and/or latitude from the original center of the region of interest described above, and then shifting the regression patterns back to all be centered at the same location and averaging. This results in computing and taking the mean of 25 regression patterns, producing a smoother picture.

286 3) Tracer budget analysis

We compute budget terms for four equations in this study: Ertel potential vorticity (EPV), relative vorticity, column-integrated internal energy, and column-integrated moisture, the equations
for which are given and discussed in Section 3. Anomalous terms for each budget are computed
by regressing each time series against the precipitation index defined above. In the case of EPV
and relative vorticity, four-dimensional fields, the time series of each term is computed explicitly;
where needed, second-order finite differences are used to estimate partial derivatives in the interior, and first-order finite differences are used to estimate partial derivatives on the boundaries. For

computing horizontal derivatives on the sphere, we follow the methods of Seager and Henderson (2013). For EPV and relative vorticity, the residuals from computing the terms explicitly are small.

For the column-integrated fields of the internal energy and moisture budgets, using a purely explicit procedure does not result in an adequately closed budget. In those cases, as an objective way of partitioning the residual, we follow the methods of Hill et al. (2017)⁴. This entails first computing an adjusted set of horizontal winds at each vertical level using the flux-form framing of the column-integrated budget to ensure things are balanced. We then use these adjusted winds to compute the horizontal advection terms in the advective form of the budget, and compute the column-integrated vertical advection term as a residual.

A useful tool to quantify the extent to which a term in an anomalous budget (X') contributes to the anomalous time tendency of a tracer (m) is projection analysis. This is a technique that has been used frequently in prior studies (e.g. in Andersen and Kuang 2011; Lutsko 2017; Adames and Ming 2018a). It entails computing the integral of the product of the term X' with the time tendency anomaly term $\frac{\partial m'}{\partial t}$ over a region A, then dividing by the integral of the square of the tendency over the same region:

$$\mathscr{P}_{X'} = \iint_A X' \frac{\partial m'}{\partial t} dA / \iint_A \left(\frac{\partial m'}{\partial t}\right)^2 dA. \tag{4}$$

Here as A we use the rectangular region 50°E to 110°E, 0° to 30°N, to approximately enclose the South Asia horizontal region. Since we are integrating only over the horizontal dimensions, if the terms are defined in the vertical, the projection, \mathcal{P} will be a function of pressure, e.g. for EPV; otherwise the projection will be a scalar quantity, e.g. for column-integrated internal energy.

⁴Note in the case of the internal energy budget the methods of Hill et al. (2017) cannot be applied exactly; therefore the budget can still not be exactly closed. Instead we follow the method described in the Appendix.

3. Results

320

322

323

325

326

327

328

329

4 a. Mean state climate

The observed JJAS mean state climate in the South Asian monsoon region has a number of distinctive attributes (Sikka 1977). We illustrate these attributes and their counterparts in the simulation in the two columns of Figure 1. Given the heavily-idealized nature of the simulation we do not expect an exact match to the real-world climate; however, we find in our simulation that several theoretically-important broad-scale features are obtained.

We first look at the JJAS-mean precipitation rate, panels (a) and (b) in Figure 1. Figure 1(a) corresponds to the 2001-2016 JJAS-mean precipitation rate computed using observations from the Tropical Rainfall Measurement Mission (TRMM) (Huffman et al. 2007) and panel (b) corresponds with JJAS-mean precipitation from our simulation. In observations, while the detailed structure is strongly influenced by small-scale features of the topography, the large-sacle structure roughly corresponds in a local shift of the Intertropical Convergence Zone (ITCZ) northward to around 20°N. This northward shift in the area of maximum time mean precipitation is roughly captured in the simulation, albeit to a lesser extent. Figure 1(b) shows that JJAS-mean precipitation maximizes at roughly 12.6°N in our simulation, with a secondary maximum located near the equator⁵.

Another notable feature of the observed climate is that column-integrated moisture increases steadily as one moves northward from the equator through the Bay of Bengal (Adames and Ming

⁵A similar double Intertropical Convergence Zone (ITCZ) structure was also found in Xie and Saiki (1999). In their idealized simulation they also found latitudinal maxima in summer precipitation in the South Asian monsoon region and near the equator. To a lesser extent a double ITCZ structure is also seen after monsoon onset in the idealized "flat" simulation of Geen et al. (2017), which uses a similarly-configured model to our simulation, with the single exception of additional of AMIP-derived slab ocean heat fluxes in their case. In our case, the double ITCZ structure is not a completely persistent feature. In other words, there are times when it is only raining in one rainband and not the other, but during July and August there are times when it rains in both rainbands simultaneously.

2018a). This is illustrated by plotting 2001-2016 JJAS-mean column-integrated water vapor from the ERA-Interim reanalysis dataset (Dee et al. 2011) in Figure 1(c). This strong gradient has been 332 theorized to play a role in the dynamics of monsoon low pressure systems (Adames and Ming 333 2018b). Figure 1(d) shows the JJAS mean column-integrated moisture in our simulation. There we can see a band of high column-integrated water vapor roughly coincident with the band of high 335 precipitation rate, running from the Arabian Sea, across India, and over the northern Bay of Ben-336 gal and Southeast Asia. Compared with reanalysis, where the water-vapor maximum is located 337 near the land-sea boundary between Bangladesh and the Bay of Bengal, the water-vapor maximum in our simulation is displaced slightly southward. In addition, column-integrated moisture mag-339 nitudes are substantially smaller than those seen in reanalysis, with maximum values of around 20 mm in our idealized simulation and around 60 mm in reanalysis (Adames and Ming 2018a). The third salient property of the mean state South Asian monsoon climate is a meridionally-342 increasing surface temperature field, and attendant easterly vertical wind shear, with westerly winds near the surface and easterly winds aloft (Xie and Saiki 1999; Boos et al. 2015; Cohen and Boos 2016). This is illustrated using 2001-2016 JJAS-mean 600 hPa temperature, and the 345 difference between the 200 hPa and 850 hPa winds from the ERA-Interim reanalysis dataset (Dee 346 et al. 2011) in Figure 1(e). The meridionally-increasing temperature gradient is induced by the 347 difference in heat capacity between the land and ocean. Because the land heats up faster than 348 the ocean, it experiences greater seasonal variation in surface temperatures than ocean at similar 349 latitudes, which gets communicated to the free troposphere. Through thermal wind balance, this positive meridional temperature gradient is associated with easterly vertical wind shear (Vallis 351

2006). The crude setup in our simulation is able to capture this, as indicated by the polewardly-

increasing 600 hPa temperature in Figure 1(f) and quiver arrows pointing from the east to the

west, indicative of easterly vertical wind shear, with strongest values of about 30 m s⁻¹ at around

352

354

12.5°N. The magnitude of the shear decreases as one moves northward over the Asian continent, which is similar to what is seen in reanalysis, e.g. in Figure 1(e). 356

b. The general character of South Asian monsoon low pressure systems in the idealized simulation

1) Dominant zonal wavenumber and frequency of precipitating disturbances Despite the simplicity of the setup of the idealized simulation, notably omitting the impacts of 359 the prominent land surface topography of Southern Asia, and the impacts of ocean heat trans-360 port, we seem to obtain an adequate South Asian JJAS mean state climate to support westward-361 propagating, precipitating disturbances. This can be made immediately apparent by looking at 362 a time-longitude diagram of unfiltered precipitation during an example summer season averaged between 7.6°N and 17.6°N, the colors in Figure 2. To guide one's eye, contour lines are added, 364 which indicate the value of the precipitation rate filtered to include data only from MLPS-like 365 modes, i.e. with zonal wavenumbers between -25 and -3 and frequencies greater than $0.067 \,\mathrm{d}^{-1}$, using the method described in Section 2.c2. In the particular season shown in Figure 2, we find 367 active westward-propagating MLPS-like activity during July, a break in August, and reinvigorated 368 activity in September. To determine the characteristic frequency and zonal wavenumber of the disturbances, we can 370 compute a frequency-wavenumber power spectrum of the precipitation rate. For the idealized 371 simulation this is shown in Figure 3(b). There we find statistically significant signal strength be-372 tween zonal wavenumbers -20 to -5, and frequencies $0.10 \,\mathrm{d}^{-1}$ to $0.35 \,\mathrm{d}^{-1}$. This pattern in signal

strength is largely consistent with that seen in daily precipitation rate observations from the Tropi-

cal Rainfall Measurement Mission (TRMM) (Huffman et al. 2007) [Figure 3(a)] and a simulation

373

374

using GFDL's AM4 (Adames and Ming 2018a) [cf. Figure 3 of Adames and Ming (2018a)]⁶, and is indicative of westward-propagating waves of alternating wet and dry periods with a horizontal scale on the order of 1000 km and a period of around 3 d to 10 d. A characteristic frequency, $\overline{f_w}$, and zonal wavenumber, \overline{k} , can be computed by taking statistically-significant-signal-weighted
means of each over the plotted domain in Figure 3:

$$\overline{f_w} = \frac{\int \int_{S \ge S_c} S f_w \, \mathrm{d} f_w \, \mathrm{d} k}{\int \int_{S \ge S_c} S \, \mathrm{d} f_w \, \mathrm{d} k}$$
 (5)

$$\bar{k} = \frac{\int \int_{S \ge S_c} Sk \, \mathrm{d}f \, \mathrm{d}k}{\int \int_{S \ge S_c} S \, \mathrm{d}f \, \mathrm{d}k},\tag{6}$$

where S is the signal strength, and S_c is the critical signal strength for statistical significance. In the observations this results in $\overline{k} = -8.7$ and $\overline{f_w} = 0.20 \, \mathrm{d}^{-1}$, while in the idealized simulation this results in $\overline{k} = -10.5$, $\overline{f_w} = 0.17 \, \mathrm{d}^{-1}$.

381

2) HORIZONTAL STRUCTURE OF PRECIPITATION, MID-LEVEL VERTICAL VELOCITY, AND LOW-LEVEL WIND ANOMALIES

The structure of the westward-propagating disturbances can be elucidated using regression analysis as described in Section 2c, following the methods of Adames and Ming (2018a). We will
first consider the horizontal structure of the anomalous precipitation, mid-level (500 hPa) vertical velocity, low-level (850 hPa) wind fields on days preceding, during, and following a storm
event centered at 80°E and the latitude of maximum mean JJAS precipitation along 80°E in the
South Asian monsoon region. In the idealized simulation, as we look at the lag sequence descending from the top of Figure 4, we can see clear evidence of a westward-propagating cyclonic
disturbance crossing the Bay of Bengal and traversing India over a span of about four days. The
disturbance is flanked by dry anticyclonic circulations. Vertical velocity anomalies slightly lead

⁶Note that the region of interest used here and in Adames and Ming (2018a) for the observations was centered at 17.5°N, rather than at 12.6°N in the case of the idealized simulation in Figure 3(b).

precipitation anomalies, similar to the disturbances analyzed in Adames and Ming (2018b). The
maximum low-level wind speed anomaly associated with the regression in the idealized experiment at lag day zero is 2.2 m s⁻¹. This value is weaker than the observed wind perturbation, which
is greater than 8.5 m s⁻¹ (Hurley and Boos 2015). This is due in part to the implicit compositing
effect of the regression analysis. Individual storms of a similar strength to the observations do
occur in the idealized simulation⁷; however a more careful analysis involving tracking individual
storms would be required to comprehensively compare the intensity distribution of the storms in
our idealized simulation to that in observations.

In comparison to regression results from GFDL's AM4, the disturbances are located farther south and have weaker precipitation anomalies, on the order of 4 mm d⁻¹ versus 10 mm d⁻¹, but have similar magnitude wind anomalies. The propagation direction is almost directly westward, the same direction as the climatological vertical wind shear [Figure 1(h)], raising the possibility that the disturbances could be adiabatically steered by the climatological mid-tropospheric winds (Boos et al. 2015).

The propagation velocity of the storms can be quantified by computing the location of the maximum vorticity anomalies at 850 hPa at each lag day. This is done by interpolating the vorticity
anomalies from the model native grid, spaced by roughly 2.8° in latitude and longitude, to a
0.1°×0.1° grid, using the nonlinear "patch" interpolation method provided by the Earth System
Modeling Framework (ESMF) (Collins et al. 2005; Zhuang and Jüling 2019). The maximum at
each lag day plotted in Figure 4 is marked with a filled black circle. We can compute an average
zonal and meridional propagation velocity over the four-day window plotted in Figure 4 for each

 $^{^{7}}$ For instance, if we compute composite means of the anomaly patterns associated with precipitation index values greater than two (approximately the strongest 3-4% of storms), we find storm-center precipitation anomalies on the order of $10 \,\mathrm{mm}\,\mathrm{d}^{-1}$, maximum wind speed anomalies near $8.5 \,\mathrm{ms}^{-1}$, and minimum surface pressure anomalies of less than $3.6 \,\mathrm{hPa}$. The results of this composite analysis are shown in Figure S2 of the supplement.

simulation by taking the difference in the position of the maximum at lag day 2 and the position of the maximum at lag day -2 and dividing by the difference in time (4 d). If we do this, we find that the average zonal propagation velocity of the maximum in the idealized simulation is $-5.9 \,\mathrm{m\,s^{-1}}$, while the average meridional propagation velocity is $-0.1 \,\mathrm{m\,s^{-1}}$. The propagation velocity in our simulation is stronger and more westward-directed than in reality (Boos et al. 2015) or in comprehensive GCMs (Adames and Ming 2018a); in both, zonal propagation velocities are typically on the order of $4 \,\mathrm{m\,s^{-1}}$ or smaller, and at least in Boos et al. (2015) there is a more significant meridional component.

c. The dynamical properties of South Asian monsoon low pressure systems in the idealized simulation

427 1) VERTICAL STRUCTURE OF ERTEL POTENTIAL VORTICITY ANOMALIES

Recent studies have illuminated the composite vertical structure of Ertel potential vorticity

(EPV) anomalies of observed MLPSs in both the pressure-longitude and pressure-latitude planes

(e.g. Boos et al. 2015; Cohen and Boos 2016). The structure of EPV can inform us about a disturbance's dynamics, e.g. Boos and Korty (2016) look at a zonal profile to assess whether moist baroclinic instability is occuring in observed MLPSs and Boos et al. (2015) look at a meridional profile to assess whether observed MLPSs could be steered westward by the JJAS mean zonal winds. To begin understanding the dynamics of of the MLPSs in our idealized simulation, we plot such profiles as well.

We compute EPV on isobars following Tamarin and Kaspi (2016):

$$q_d = -g \left(f \hat{\mathbf{k}} + \nabla \times \mathbf{u} \right) \cdot \nabla \theta, \tag{7}$$

where all horizontal derivatives are computed on surfaces of constant pressure, and in spherical coordinates. $\mathbf{u}=(u,v,\boldsymbol{\omega})$ is the three-dimensional wind velocity in pressure coordinates, $\hat{\mathbf{k}}$ is the vertical unit vector, f is the Coriolis parameter, g is the gravitational acceleration, and θ is the potential temperature. Horizontal derivatives are computed using second-order centered finite differences following the methods described in Seager and Henderson (2013). Vertical derivatives are computed using second-order centered finite differences in the interior and first order finite differences on the boundaries. We scale q_d by 10^6 such that it has units of potential vorticity units (PVU).

If we compute EPV using six-hourly output, regress it onto the precipitation index at lag day 445 zero, and average the result over the latitudes of the region of interest, the result is Figure 5(a), a zonal cross-section of anomalous EPV for MLPSs in our idealized simulation. Overlaid are 447 contours representing a similarly obtained cross section of temperature anomalies. Associated 448 with MLPSs we find a slightly westward-tilting, i.e., in the direction of the shear vector plotted in 449 Figure 1(f), column of anomalous positive EPV centered at around 80°E and 600 hPa. The positive EPV anomalies are flanked to the west and east by weaker negative EPV anomalies, with similar 451 tilts. Positive temperature anomalies can be found above and slightly to the east of the positive 452 EPV anomalies, centered at around 82°E and 400 hPa, while negative temperature anomalies can 453 be found to the west and east as well as below the central warm core. While the anomalies are 454 weaker, the zonal profiles of temperature and EPV anomalies obtained in our idealized simulation 455 qualitatively match those of observed MLPS shown in Cohen and Boos (2016), though they lack the characteristic bimodality of the EPV profile of MLPSs in the vertical noted by Hurley and Boos 457 (2015) and Cohen and Boos (2016) in the ERA-Interim reanalysis dataset and Hunt and Turner 458 (2017) in simulations using the Met Office Unified Model (MetUM). This could be due in part to the coarser vertical resolution used in our idealized simulation (40 vertical levels), when compared 460

with the vertical resolution used in ERA-Interim (60 vertical levels) (Dee et al. 2011) or MetUM (85 vertical levels) (Hunt and Turner 2017).

Taking the same EPV anomalies obtained through regression, but this time averaging between 75°E and 85°E, we can obtain a profile of the composite disturbance in the pressure-latitude plane.

This is shown in Figure 5(b). Following Boos et al. (2015) we also plot contour lines representing the mean JJAS zonal winds averaged over the same longitudinal region as the EPV anomalies. In Figure 5 we find that the bulk of the disturbance, identified as the region of positive EPV anomalies, is located in a region of westerly winds (solid contours). At upper levels, there is some overlap between positive EPV anomalies and easterly winds; however, the magnitude of the easterly winds are fairly weak in the region of overlap.

2) Anomalous Ertel Potential Vorticity Budget

We can learn more about the propagation mechanism of the MLPSs in our idealized simulation
by computing anomalous tracer budgets. We will start with the anomalous EPV budget associated
with the storms; a similar analysis was done for a single particular storm in Boos et al. (2015),
though here our anomalies represent a composite obtained through regression.

An equation governing the time tendency of EPV is given in Tamarin and Kaspi (2016):

$$\left(\frac{\partial q_d}{\partial t}\right)' = -\left(\mathbf{u} \cdot \nabla q_d\right)' - g\left[\boldsymbol{\eta} \cdot \nabla \left(\frac{\mathrm{d}\boldsymbol{\theta}}{\mathrm{d}t}\right)\right]'. \tag{8}$$

The first term on the right hand side of Equation 8 corresponds with the EPV tendency associated with advection of EPV and the second term corresponds to the EPV tendency due to diabatic processes. $\eta = f\hat{\bf k} + \nabla \times {\bf u}$ is the three-dimensional absolute vorticity vector. The advection term

⁸Note that in Boos et al. (2015) the zonal wind was smoothed with a 21-day running mean and then composited over storms; here we use the full climatological mean rather than a smoothed composite.

can be separated into horizontal and vertical components:

$$-\left(\mathbf{u}\cdot\nabla q_{d}\right)' = -\left(\mathbf{v}\cdot\nabla_{p}q_{d}\right)' - \left(\omega\frac{\partial q_{d}}{\partial p}\right)' \tag{9}$$

It follows that under adiabatic processes, EPV is conserved following the flow.

Spatial patterns of the different terms in Equation 8 at the 500 hPa and 700 hPa levels are shown 482 in Figure 6. There we find that the pattern of anomalous EPV time tendency [panels (a) and 483 (f)] is consistent with the westward-propagation of the storms, with positive EPV tendencies to 484 the west of the vortex center and negative EPV tendencies to the east at either level. As Boos et al. (2015) found in a case study of a monsoon depression, in the mid-troposphere a negative 486 diabatic tendency at the storm center [Figure 6(b)] is largely compensated for by a positive vertical 487 advection tendency in the same location [Figure 6(d)]. At this level in Boos et al. (2015) and in our simulation, anomalous horizontal advection of EPV [Figure 6(c)] appears to project most 489 strongly onto to the spatial pattern of the overall EPV tendency. Closer to the surface, at 700 hPa, 490 diabatic processes appear to play a larger role in the propagation tendency [cf. Figure 6(g) and Figure 6(h)], with horizontal advection no longer being as significant; again this is similar to what 492 is found in Boos et al. (2015) in reanalysis. The residual in the budget at each level, shown in 493 Figure 6(e) and 6(j), is small compared to the explicitly computed terms. While the results plotted in Figure 6 provide qualitative evidence of the importance of hori-495 zontal advection and diabatic processes in the propagation of EPV anomalies, we can be more 496 quantitative about this assessment by applying projection analysis, described in Section 2c, to the 497

EPV budget. The projections for each term at each vertical level in the idealized simulation are

shown in Figure 7. Here it is quantitatively clear that anomalous horizontal advection of EPV

is dominant in the mid-to-upper troposphere, while diabatic processes, primarily condensation of

499

water vapor⁹, become more important in the lower troposphere, i.e. near 700 hPa. This is qual-501 itatively consistent with the results of Boos et al. (2015). Vertical advection anomalies have a small negative contribution to the EPV tendency in the lower troposphere and a small positive 503 contribution in the mid-to-upper troposphere; in general they tend to oppose the diabatic tendency 504 throughout the atmosphere. In doing a Reynolds decomposition, a technique described in the next paragraph, of the vertical advection term (Figure S4), we find that at 500 hPa the product of the high frequency vertical velocity and low frequency vertical gradient of EPV term, $\left(\omega' \frac{\partial \overline{q_d}}{\partial p}\right)'$, is the 507 largest term, with the term representing the product between the low-frequency vertical velocity and high-frequency vertical gradient of EPV, $\left(\overline{\omega} \frac{\partial q'_d}{\partial p}\right)'$, being 1/3 of its amplitude, and the other 509 terms playing a negligible roles. At the 700 hPa level, $\left(\overline{\omega} \frac{\partial q'_d}{\partial p}\right)'$ and $\left(\omega' \frac{\partial \overline{q_d}}{\partial p}\right)'$ have a more equal role, with the other terms playing secondary roles. Because, particularly in the mid-troposphere, the spatial pattern of the vertical advection term is largely collocated with the storm-center EPV 512 anomalies, this suggests that the low-frequency vertical gradient in EPV has a role in the growth and maintenance of the storms. 514

Horizontal advection consists of two quadratic terms in the budget, one zonal and one meridional. It is worth asking if these terms could potentially be treated as being linear in high-frequency
factors, i.e. either linear in a high frequency wind factor or linear in a high-frequency EPV-gradient
factor, or whether the anomalous horizontal advection tendency is nonlinear process, i.e. representing advection of high-frequency EPV anomalies by the high-frequency horizontal flow. At
least for stronger storms, Boos et al. (2015) suggest that nonlinear processes are at work. To see if

⁹We conclude this by computing the component of the anomalous diabatic EPV tendency due to condensation via Equation 5 of Tamarin and Kaspi (2016), which is based on the work of Emanuel et al. (1987) (Figure S3). We find that it closely resembles the anomalous pattern of the total diabatic EPV tendency over the regression index region, representing 71% of it at the 700 hPa level and 97% of it at the 500 hPa level. The dominance of condensation of water vapor in the diabatic heating component of the EPV tendency is qualitatively consistent with composites of observed MLPSs (Hunt et al. 2016b).

this is the case in our idealized simulation we can perform a Reynolds decomposition on the terms associated with horizontal advection:

$$-(\mathbf{v}\cdot\nabla q_{d})' = -\frac{1}{a\cos\phi}\left(\overline{u}\frac{\partial\overline{q_{d}}}{\partial\lambda} + \overline{u}\frac{\partial q_{d}'}{\partial\lambda} + u'\frac{\overline{\partial q_{d}}}{\partial\lambda} + u'\frac{\partial q_{d}'}{\partial\lambda}\right)'$$
$$-\frac{1}{a}\left(\overline{v}\frac{\partial\overline{q_{d}}}{\partial\phi} + \overline{v}\frac{\partial q_{d}'}{\partial\phi} + v'\frac{\overline{\partial q_{d}}}{\partial\phi} + v'\frac{\partial q_{d}'}{\partial\phi}\right)'. \quad (10)$$

Above we have taken the quadratic advection terms and broken them down into terms that are linear in high-frequency factors and terms that are nonlinear in high-frequency factors. Similar to the method used in (Adames and Ming 2018b), overbars represent low-frequency factors, obtained by spectrally filtering the data to contain frequencies less than 0.067 d⁻¹ per day, while primed factors represent the quickly varying residual. Because the overbar factors still vary in time, it is possible the product of two low-frequency fields could project non-negligibly onto the precipitation index¹⁰; therefore we retain those terms in the equation above. Note, as described in Section 2, we filter all products to contain frequencies greater than 0.067 d⁻¹ per day before regressing.

Projecting each term onto the total EPV tendency, we find, as was qualitatively shown in Figure 5(b), that advection of high-frequency EPV by the low-frequency zonal wind tends to work
against the prevailing westward-propagating tendency of EPV in the lower-to-mid troposphere, the
solid red line in Figure 8. Instead, the most important term is the advection of the low-frequency
EPV by the high-frequency meridional winds, the dashed blue line in Figure 8. Because the highfrequency meridional winds are cyclonic, they blow southward to the west of the storm, down the
low-frequency EPV gradient, bringing high mean EPV air from the north, and northward east of

¹⁰Consider the idealized example of two factors that can be described as a sine and cosine wave of the same frequency, ω . Their product, via the sine double angle identity, would then be a sine wave with twice the frequency, e.g. $\sin(\omega t)\cos(\omega t) = \frac{1}{2}\sin(2\omega t)$, which could project onto a higher frequency index.

the storm up the low frequency EPV gradient, bringing low mean EPV air from the south, resulting in the dipole pattern seen in Figure 6(a). This is consistent with the propagation mechanism of linear Rossby waves.

The other terms, related to advection of low-frequency EPV by the low-frequency horizontal winds, advection of high-frequency EPV by the low-frequency meridional winds, advection of the low-frequency EPV by the high-frequency zonal winds, and advection of the high-frequency EPV by the high-frequency horizontal winds play a negligible role in the propagation of EPV anomalies in the lower troposphere, and play minor offsetting roles in the upper troposphere. The tertiary role of high-frequency EPV advection by the high-frequency horizontal winds in the budget in particular suggests that beta drift is not a primary driver of propagation for the storms in our simulation.

Further insight into the dynamics of the MLPSs in our idealized simulation can be gleaned from analysis of the budgets of vorticity, column-integrated internal energy, and column-integrated moisture. By looking at these budgets, we can approximately determine whether a simplified model, like moisture vortex instability (Adames and Ming 2018a), could be used to describe the storm systems in our simulation.

555 3) Anomalous vorticity budget

556

The anomalous flux-form vorticity equation discussed in Boos et al. (2015) is given by:

$$\frac{\partial \zeta'}{\partial t} = -\left[\nabla \cdot \left(f + \zeta\right)\mathbf{u}\right]' - \nabla \cdot \left(\omega \hat{\mathbf{k}} \times \frac{\partial \mathbf{u}}{\partial p}\right)'. \tag{11}$$

In this budget, $-\nabla \cdot f \mathbf{u}$ represents the collective influence of vortex stretching and horizontal advection involving the planetary vorticity, $-\nabla \cdot \zeta \mathbf{u}$ represents the collective influence of vortex stretching and horizontal advection involving the relative vorticity, and $\nabla \cdot \left(\omega \hat{\mathbf{k}} \times \frac{\partial \mathbf{u}}{\partial p}\right)$ represents the collective influence of vertical vorticity advection and vortex tilting. It is useful to view the

spatial anomaly patterns of the budget terms through this decomposition, because it separates terms into two categories. The first category consists of terms that are definitively linear in highfrequency factors and are not impacted by the low-frequency winds; only $-\nabla \cdot f \mathbf{u}$ belongs in this category.

The second category consists of terms that may contain components nonlinear in highfrequency factors and/or influence of the low-frequency winds; $-\nabla \cdot \zeta \mathbf{u}$ and $\nabla \cdot \left(\omega \hat{\mathbf{k}} \times \frac{\partial \mathbf{u}}{\partial p}\right)$ are the terms in this category.

The terms in the anomalous budget for a level in the upper troposphere (400 hPa) and a level in the lower troposphere (850 hPa), decomposed as described above, are shown in Figure 9. Panels (a) and (e) shows the anomalous time tendency of the relative vorticity. There we can see a dipole pattern oriented along an east-west axis, similar to what we see in the anomalous EPV budget. In addition we can see that the dominant term on the right hand side of Equation 11 is the term involving the planetary vorticity. Terms potentially involving the low-frequency winds, i.e. $-\nabla \cdot (\zeta \mathbf{u})'$ or $-\nabla \cdot (\omega \hat{\mathbf{k}} \times \frac{\partial \mathbf{u}}{\partial p})'$, are about an order of magnitude smaller at both 850 hPa and 400 hPa, and to some extent offset each other.

Figure 10 shows the projection of the vorticity budget terms on the time tendency of relative vorticity in the idealized simulation. There we can see that our budget closes nearly perfectly below about 500 hPa and only slightly diverges above, as evidenced by the dashed black line, representing the total of the terms on the right hand side of Equation 9 having a projection of about one at all pressure levels. In addition, we see quantitative evidence of the dominance of the planetary vorticity term, the red line in Figure 10, which indicates a spatial projection of over 0.5 below 300 hPa. It is only above 300 hPa anomoalous vortex stretching associated with the relative vorticity and/or anomalous relative vorticity advection, $-\nabla \cdot \zeta \mathbf{u}$, becomes of leading-

 $^{^{11}}$ Note that since we highpass filter all quantities before regressing, as described in Section 2.c, any low-frequency component of \mathbf{u} will be filtered out.

order significance in the budget. The combined effects of anomalous vertical advection and vortex tilting do not project strongly onto the time tendency of relative vorticity – in other words, they do not contribute to the propagation of vorticity anomalies anywhere in the troposphere – though they may play a role in their growth and maintenance, because of their approximate collocation with vorticity anomalies themselves.

4) Anomalous column-integrated internal energy budget

Models of transient disturbances in the tropics can often be simplified by assuming a firstbaroclinic mode vertical structure. This allows one to effectively remove the vertical dimension
from the problem and construct a two-dimensional shallow-water-like models, where the relevant internal energy and moisture budgets are vertically-integrated (e.g. Neelin and Zeng 2000;
Adames and Kim 2015; Adames and Ming 2018a). To understand the importance of terms in
these anomalous budgets, particularly in the context of these simplified models, we therefore look
at their vertically-integrated forms.

Following Neelin (2007), the terms in the anomalous vertically-integrated internal energy equation are written below:

$$C_{p} \frac{\partial \left\{T\right\}'}{\partial t} = -C_{p} \left\{\mathbf{v} \cdot \nabla T\right\}' - \left\{\omega \frac{\partial s}{\partial p}\right\}' + P' + F' + H'. \tag{12}$$

Here C_p is the specific heat of dry air at constant pressure; T is the temperature; $s = C_pT + gz$ is the dry static energy; P is heating due to condensation of water vapor associated with precipitation; F is the net column radiation; and H is the sensible heat flux. The curly braces signify mass-weighted integration over the full column of the quantity inside:

$$\left\{ (\cdot) \right\} = \frac{1}{g} \int_0^{p_s} (\cdot) \, \mathrm{d}p. \tag{13}$$

Ultimately, the net radiation and sensible heat terms in the anomalous budget make negligible contributions to the total; therefore we plot the anomalous terms of the following approximate form of the budget:

$$C_{p} \frac{\partial \left\{T\right\}'}{\partial t} \approx -C_{p} \left\{\mathbf{v} \cdot \nabla T\right\}' - \left\{\omega \frac{\partial s}{\partial p}\right\}' + P', \tag{14}$$

which is exactly the same as Equation 12 with the exception of our ignoring of F' and H'. For a comprehensive plot of the spatial pattern of the all of the anomalous terms in the column-integrated internal energy budget, including F' and H', as well as a Reynolds decomposition of the horizontal advection term, performed following the methodology used for the EPV budget, see Figure S5 in the supplement.

The terms in the approximate budget are plotted in Figure 11 along with contours indicating the 610 values of anomalous vertically-integrated internal energy, $C_p\{T\}'$. In Figure 11(a) we can see a 611 negative anomaly in internal energy at the storm center, flanked by an anomalous negative internal energy tendency to the west and an anomalous positive internal energy tendency to the east; this dipole pattern in the tendency is consistent with the westward propagation of the negative internal energy anomaly at the storm center. The term on the right hand side of the budget that projects most strongly onto the time tendency is the sum of the vertical advection of dry static energy and 616 the column-integrated latent heating associated with precipitation [Figure 11(c)]; overall this has a 617 projection value of 2.65 on the tendency over the domain plotted. Horizontal advection of internal energy serves to damp this propagation tendency [Figure 11(b)]. Total horizontal advection has 619 a projection value of -1.45. Of this damping influence, horizontal advection of low-frequency 620 internal energy by the high-frequency meridional wind, $-\frac{C_p}{a} \left\{ v' \frac{\partial \overline{T}}{\partial \phi} \right\}'$, and horizontal advection of the high-frequency internal energy by the low-frequency zonal wind, $-\frac{C_p}{a\cos\phi}\left\{\overline{u}\frac{\partial T'}{\partial\lambda}\right\}'$, con-622 tribute -1.18 and -0.16 to the projection, respectively, indicating that the horizontal advection 623 term is primarily due to the high-frequency meridional wind acting on the low-frequency meridional temperature gradient. The low-frequency meridional temperature gradient is positive due to the imposed the land-ocean contrast in heat capacity, though slightly weaker than the observed meridional temperature gradient as shown in Figure 1(e) and (f). The small contribution of the $-\frac{C_p}{a\cos\phi}\left\{\overline{u}\frac{\partial T'}{\partial\lambda}\right\}'$ term is due to the westward advection of the upper-level temperature anomalies by the low-frequency upper-level easterly winds, e.g. in Figure 5. The residual term is plotted in Figure 11(d); there it is clear that while the anomalies do project negitively onto the spatial pattern of the time tendency, the magnitudes of the anomalies are small. A full tabulation of the projections of each term in the decomposed internal energy budget (Equation 12) can be found in Figure 12.

5) Anomalous column-integrated moisture budget

Following Adames and Ming (2018a), the anomalous column-integrated moisture budget can be written as:

$$L_{v} \frac{\partial \left\{q_{v}\right\}'}{\partial t} = -L_{v} \left\{\mathbf{v} \cdot \nabla q_{v}\right\}' - L_{v} \left\{\omega \frac{\partial q_{v}}{\partial p}\right\}' - P' + E'. \tag{15}$$

Here q_{ν} represents the specific humidity and P' and E' represent the precipitation and evaporation, respectively, each implicitly scaled by L_{ν} , the latent heat of vaporization, to have units of W m⁻² to be consistent with the convention used in the internal energy equation. The theory of Adames and Ming (2018b) assumes that of the terms in the anomalous budget in Equation 15, only the horizontal advection of the low-frequency moisture by the high-frequency meridional winds, vertical advection of moisture, and precipitation anomalies are important. It is worth verifying whether this is true in our simulation.

Again, we compute the terms in the anomalous budget following the methods described in Section 2c.3. The results are shown in Figure 13. The time tendency anomaly pattern, panel (a), depicts an east-west-oriented dipole pattern, consistent with the westward propagation of the storms.

The two largest terms on the right hand side of the budget are the vertical advection and precipitation terms, each with maximum magnitudes on the order of 60 W m⁻², with vertical advection 648 being a net source (positive) and precipitation being a net sink (negative). Since they largely offset 649 each other, as in Adames and Ming (2018a), we combine these into one term and refer to it as the 650 "column moisture process." This aggregate term projects strongly onto the time tendency, with 651 a projection value of 0.63 over the region plotted, though perhaps has a slightly northwestward 652 orientation compared with the more westward orientation of the tendency itself. Horizontal ad-653 vection plays a secondary role, and acts to turn the dipole orientation more toward the west (with a projection value of 0.42). In terms of propagation, the anomalous latent heat fluxes, panel (d), 655 play a minor damping role, with a projection of -0.05; however they are positive, and collocated 656 mainly with the column moisture anomalies associated with the disturbance, and therefore more 657 directly contribute to their in-place amplification. In the projection sense, these results are largely 658 consistent with the results of Adames and Ming (2018a) in AM4; there the column moisture pro-659 cess term was dominant, with a minor positive contribution coming from horizontal advection, and a minor negative contribution coming from evaporation. 661

Similar to what we did with the EPV and internal energy budgets, we can decompose the horizontal advection term into components due to the product of the low-frequency winds and high-frequency moisture gradients, products of the high-frequency winds and the low-frequency moisture gradients, and products of the high-frequency factors. This allows us to continue to determine the feasibility of using a linear model of the column-integrated moisture equation. The spatial patterns of the terms associated with this decomposition compared with all other terms in the anomalous column-integrated moisture budget can be found in Figure S6 of the supplement. For brevity, we show only the projection of each of these terms on the anomalous time tendency of column-integrated moisture in the main body of this manuscript in Figure 14. Here we find

that the primary reason for the positive contribution of the horizontal advection of moisture to the westward-propagation tendency is the component due to advection of high-frequency mois-672 ture anomalies by the low-frequency zonal winds, with a projection of 0.12. This is followed in 673 projection magnitude by the term related to the product of the high-frequency meridional wind 674 and high-frequency meridional moisture gradient, 0.08, and the term related to the product of the low-frequency meridional wind and high-frequency meridional moisture gradient, 0.07. We will 676 note, however, that the term nonlinear in high-frequency factors is not statistically significant over 677 a large portion of the South Asian monsoon region [see Figure S6(h)]. The term related to the product of the high-frequency meridional winds and low-frequency meridional moisture gradient 679 has a strong spatial pattern relative to the other terms that comprise the total horizontal advection term [Figure S6(g)]; however, it does not project strongly onto the anomalous tendency of column-681 integrated moisture. This could be due to the fact that the MLPSs in our idealized simulation are 682 centered at roughly the local maximum in the JJAS-mean column-integrated moisture field, which 683 coupled with a cyclonic circulation leads to the quadrupole pattern seen in Figure S6(g).

4. Discussion

- We can assess the potential applicability of various theories that have appeared in the literature for the growth and propagation of MLPSs to the storms we find in our idealized simulation by interpreting the structure and budget analysis results presented above.
- a. Advection by the mean upper-level easterly winds, modified by beta drift
- We will begin by discussing one possible propagation mechanism, inspired by the notion that MLPSs could be analogous to tropical depressions (Boos et al. 2015; Cohen and Boos 2016).

 Here it is suggested that MLPSs could be steered westward by the low-frequency upper-level

easterly winds, and have an additional northward component to their motion through beta drift, 693 i.e. nonlinear advection of high-frequency vorticity anomalies by the high-frequency winds. Boos 694 et al. (2015) base this hypothesis off of a composite analysis of South Asian monsoon depressions 695 using tracks and positions from their own archive (Hurley and Boos 2015) and meteorological variables derived from the ERA-Interim reanalysis (Dee et al. 2011). In looking at the structure of 697 EPV anomalies of the storms in our simulation in the pressure versus latitude plane, with the JJAS 698 mean zonal winds overlaid, Figure 5(b), we find that steering by the mean upper-level easterly 699 winds is likely not the case for our disturbances. The majority of the positive EPV anomalies are located in a region of mean westerly winds, and where there is overlap with easterly winds, the 701 winds are too weak to propagate the vortex westward at $6 \,\mathrm{m \, s^{-1}}$. 702

Beta drift is indicative of nonlinear advection of high-frequency EPV anomalies by highfrequency wind anomalies and is normally responsible for a meridional component to a storm's
path (Tamarin and Kaspi 2016), which indeed is significant for depressions seen in observations
(Hurley and Boos 2015; Boos et al. 2015). In our analysis, we find that there is little nonlinear
contribution to the anomalous horizontal advection term in the EPV budget, which suggests that
beta drift is not playing a major role in the propagation of the storms either. This is consistent with
the fact that the storms have little northward component to their propagation, which is a deviation
from those in observations (Hurley and Boos 2015).

11 b. Baroclinic instability

Some of the original theories for MLPSs were based in the idea that they emerged out of dry or moist baroclinic instability in the presence of an easterly vertical wind shear (Mishra and Salvekar 1980; Mak 1983; Moorthi and Arakawa 1985). Indeed this type of mechanism has been used to explain MLPS-like disturbancs that occurred in a similarly idealized model roughly twenty years

ago (Xie and Saiki 1999). Cohen and Boos (2016) argue, however, based on the structure of EPV anomalies in the pressure-longitude plane, that moist baroclinic instability is not occurring 717 in observed MLPSs. They argue that in order for counterpropagating Rossby waves to interact 718 constructively, their phasing must be such that EPV anomalies tilt against the mean vertical wind 719 shear with height; in other words, EPV anomalies would need to tilt to the east in the South Asian 720 monsoon region with its characteristic mean easterly shear. This is not the case in observations 721 (Cohen and Boos 2016), and it is also not the case for the storms in our idealized simulation. 722

We find that the structure of EPV and temperature anomalies shown in Figure 5(a) resembles that 723 found for monsoon depressions in Cohen and Boos (2016). There, for storms mid-way through 724 their lifetimes, Cohen and Boos (2016) found that monsoon depressions can be characterized by 725 a positive column of EPV, tilting slightly westward with height, i.e. with the shear, and a warm-726 over-cold temperature anomaly structure. They contrast these anomaly patterns with those seen 727 for extratropical diabatic Rossby waves, noting in particular that diabatic Rossby waves have EPV 728 anomalies that tilt against the mean wind shear, a necessary condition for growth out of baroclinic instability. Because the positive EPV anomalies in our idealized simulation tilt with the shear¹², 730 we take Figure 5(a) as tentative evidence that baroclinic instability is not playing a role in the life cycle of the low pressure systems simulated in our idealized model.

731

¹²Above the 200 hPa pressure level there is a strong positive EPV anomaly slightly the east of the mid-tropospheric EPV anomalies, and a negative anomaly directly above the mid-troposphere maximum. It is possible one could interpret these as evidence of tilting against the shear, and thus possible baroclinic instability, following the argument of Cohen and Boos (2016). However, while not apparent in Figure 5(a) due to the statistical significance mask, these anomalies appear rather to be components of a more organized packet of gravity waves propagating upward from the monsoon low pressure system, similar to those seen emanating from convectively coupled waves near the equator (Kiladis et al. 2009), and not part of the low pressure system itself.

733 c. Moisture vortex instability

Despite baroclinic instability appearing not to play a role in the disturbances in our idealized simulation, their propagation, at least at upper levels, appears to be consistent with the propagation mechanism of Rossby waves, i.e. advection of the planetary vorticity by the anomalous meridional winds. At lower levels, analysis of the anomalous EPV budget suggests that propagation is driven by latent heat release due to the condensation of water vapor associated with precipitation. Superficially, this is consistent with another recently proposed theory for MLPSs, called "moisture vortex instability" (MVI) (Adames and Ming 2018a).

Moisture vortex instability theory is based on using vertically-truncated versions of the momen-741 tum, thermodynamic, and moisture equations; in this context "vertically-truncated" means that 742 the horizontal winds, temperature, geopotential, and specific humidity are projected onto basis 743 functions consistent with a first-baroclinic mode vertical structure for the vertical velocity. This reduces the equations to a shallow water-like system, which is more amenable to analysis [e.g. as 745 in Neelin and Zeng (2000), Haertel et al. (2008), or Adames and Kim (2015)]. In Adames and 746 Ming (2018b), the truncated equations are linearized about a South Asian monsoon-season-like basic state, and through analysis of a dispersion relation, are shown to support unstable modes. 748 The instability is associated with a partially in-phase relationship between precipitation anomalies 749 (corresponding with upward vertical motion and convergence of low-level horizontal winds) and 750 cyclonic (i.e. positive) vorticity anomalies. The precipitation anomalies, through their associa-751 tion with low-level convergence, result in a growing tendency for the vorticity anomalies through 752 vortex-stretching (Adames and Ming 2018b). Propagation of the wave in their framework is primarily due to vortex stretching from moist convection in regions of isentropic ascent and horizontal 754 moisture advection.

In terms of the primitive equations, moisture vortex instability theory depends on the advection
of planetary vorticity, vortex stretching, meridional and vertical advection of the mean internal
energy and moisture by the anomalous winds and latent heating due to precipitation. It assumes
no influence by the mean state winds or terms nonlinear in anomalies (Adames and Ming 2018a).
Our analysis of the anomalous vorticity, column-integrated internal energy, and column-integrated
moisture budgets can shed light on whether the assumptions made in constructing the theory hold
in our idealized simulation.

In the case of the vorticity budget, we find that at both 850 hPa and 400 hPa that propagation is 763 dominated by the terms associated with advection of planetary vorticity and vortex stretching, i.e. 764 the term $-\nabla \cdot (f\mathbf{u})'$, which is consistent with MVI theory. The term related to the influence of the 765 collective influence of vertical vorticity advection and vortex tilting, i.e. $-\nabla \cdot \left(\omega \hat{\mathbf{k}} \times \frac{\partial \mathbf{u}}{\partial p}\right)'$ does project strongly onto relative vorticity anomalies at 400 hPa, however, which suggests that it plays 767 a role in the growth and maintenance of vorticity of the MLPSs in our simulation, which is not 768 consistent with MVI. This term happens to be dominated by the contribution of the divergence of the product between the anomalous vertical velocity and the low-frequency vertical shear of the 770 winds (not shown), indicating the potential importance of including the low-frequency winds in a 771 theory for MLPSs. 772

In the case of the column-integrated internal energy budget, the picture of the storms in our simulation is largely consistent with the assumptions of MVI theory. There the anomalous radiative
and sensible heating parts of the thermodynamic equation were neglected, and they are indeed
found to be negligible in our simulation. The terms retained in the anomalous thermodynamic
budget in Adames and Ming (2018a) were the vertical advection of mean dry static energy by the
anomalous pressure velocity, the column latent heating due to precipitation, and meridional ad-

vection of mean internal energy by the anomalous meridional wind. These are indeed the leading order terms in the anomalous thermodynamic budget in our simulation (see Figure 12).

Finally, as assumed in Adames and Ming (2018b), the vertical advection of moisture and the loss 781 of column moisture through precipitation play an important role in the moisture budget. That said, 782 assumptions made regarding the horizontal advection of moisture in Adames and Ming (2018b) do 783 not necessarily hold in our simulation. Adames and Ming (2018b) assume that advection of mean 784 moisture by the anomalous meridional wind plays a leading-order role in the budget. We find 785 that this does not quite hold in our simulation. While the advection of low-frequency moisture by the high-frequency meridional wind anomalies has a relatively strong magnitude relative to 787 other terms related to horizontal advection, it does not project strongly onto the anomalous time 788 tendency of column-integrated moisture. This is likely in part because the storms we analyze 789 in this simulation are centered roughly at the latitude of maximum JJAS-mean column-integrated 790 moisture, in contrast to the assumption made by Adames and Ming (2018a), that the storms form in 791 an area of uniformly increasing column moisture in the meridional direction. A term that projects more strongly is the advection of the high-frequency moisture anomalies by the low-frequency 793 zonal wind, which was not considered in Adames and Ming (2018a). 794

795 5. Conclusion

In this study we have completed a systematic analysis of low pressure systems in the South
Asian monsoon region in a heavily-idealized moist GCM, notably without impacts of clouds or
topography. The low pressure systems found in our simulation share a number of characteristics with South Asian monsoon low pressure systems observed in reality and those simulated in
GFDL's AM4. For example precipitation anomalies in the South Asian monsoon region in our
simulation have a typical zonal scale of around zonal wavenumber 10, consistent with the scale

seen in TRMM observations and AM4; the typical frequency of around 0.2 d⁻¹ is consistent with that found in those datasets as well (Adames and Ming 2018a). In addition, we find that the vertical structure of potential vorticity anomalies associated with the low pressure systems simulated in our model shares an important qualitative feature with that found in reanalysis: the EPV anomalies in the troposphere tilt slightly with the JJAS mean easterly zonal wind shear (Cohen and Boos 2016).

Aspects of the low pressure systems that differ slightly from those seen in reality are their prop-808 agation speed and direction. In our simulation, the storms propagate predominantly westward at speeds of over 6 m s⁻¹; this is faster than storms seen in GFDL's AM4 and reanalysis. There are 810 several possible explanations for this difference. Two of these arise from Rossby wave theory. 811 From inspection of Figure 4 it is possible that these waves are of slightly larger scale, resulting in a smaller horizontal wavenumber, than the low pressure systems simulated in AM4 and observed 813 in reanalysis. In addition, because these systems occur at a lower latitude than in the aforemen-814 tioned datasets, the Rossby radius of deformation is larger, which would also cause these systems to exhibit faster westward propagation [see Equation 22a in Adames and Ming (2018b)]. We find 816 little meridional component to the propagation direction, which is different than at least reanalysis 817 Boos et al. (2015); in GFDL's AM4 model, storms propagated predominantly westward as well. It is possible that the northward component of propagation is largely a result of nonlinear beta drift, 819 which is characteristic of the stronger storms that were analyzed by Boos et al. (2015). Per the 820 role of the meridional temperature gradient in the propagation of column-integrated moist enthalpy 821 anomalies associated with MLPSs suggested by moisture vortex instability theory (Adames and 822 Ming 2018a), the more equatorward location of the systems when compared with observations 823 may be in part due to the more equatorward meridional temperature gradient in our simulation.

The movement of the weak disturbances in our simulation can largely be explained through 825 linearized versions of the primitive equations, rather than beta drift, as was the case for monsoon 826 depressions analyzed in reanalysis in Boos et al. (2015). A slight deviation from moisture vortex 827 instability theory is the potential contribution of the vertical shear of the low-frequency winds to the growth and maintenance of the disturbances. Despite not being classic examples of baroclinic 829 instability, these disturbances might still be classified as a certain form of diabatically-influenced 830 Rossby wave, like that described in Adames and Ming (2018b). A major distinguishing factor 831 between extratropical diabatic Rossby waves and Rossby-like waves deriving from moisture vortex instability is that, while influenced by moist processes, extratropical Rossby waves can grow in 833 the absence of precipitation (Vallis 2006); for moisture vortex instability, precipitation is necessary for growth (Adames and Ming 2018b). The possibility of an approximate explanation via a linear model could motivate further sensitivity studies in a modeling framework similar to the one used 836 here, to test whether properties of the mean state, like the meridional temperature or moisture 837 gradient, could influence properties of the low pressure systems, like the phase speed.

While the work we have done here demonstrates that somewhat realistic MLPS-like disturbances can be simulated with simplified model physics and boundary conditions, it does not rule out that even further idealizations could be made. We intentionally used realistic continental geometry, reduced heat capacity, and a bucket hydrology model to limit evaporation over land, as to remove those as possible reasons for too unrealistic a mean climate to support MLPSs. In future work it could be useful to run simulations with realistic continental geometry, with only reduced heat capacity over land, or only bucket hydrology over land to see which is most important in generating a mean state climate suitable for South Asian MLPSs. For example, this could inform us whether it might be valuable to use a simpler land setup such as the "moist land" simulations with a rectangular continent in Zhou and Xie (2018) when attempting to systematically modify the mean state

839

840

842

843

845

as suggested at the end of the previous paragraph. In those simulations in Zhou and Xie (2018), the continental geometry is significantly simplified, and the land surface is assumed to always be saturated; that is, the only thing distinguishing land from ocean is its reduced heat capacity. 851 We thank Steve Garner, Gan Zhang, and three anonymous reviewers for help-Acknowledgments. ful comments on earlier versions of this manuscript, as well as Spencer Hill for discussions and 853 resources regarding methods for computing closed column-integrated tracer budgets. S. K. C. was 854 supported by a National Defense Science and Engineering Graduate Fellowship. A. F. A. was supported by the University of Michigan's startup package and by the National Science Foundation's 856 grant ATM 1841559. The output from the simulations described in this manuscript is archived at 857 the Geophysical Fluid Dynamics Laboratory and is available upon request.

APPENDIX

860

Method for computing the internal energy budget

To compute the terms in Equation 12, we start from the dry static energy budget, which has a similar form:

$$\frac{\partial \{s\}}{\partial t} = -\{\mathbf{v} \cdot \nabla s\} - \left\{\omega \frac{\partial s}{\partial p}\right\} + P + F + H. \tag{A1}$$

Unlike Equation 12, however, the advection terms can be placed in flux form:

$$\frac{\partial \{s\}}{\partial t} = -\nabla \cdot \{\mathbf{v}s\} + P + F + H. \tag{A2}$$

With the budget in this form, we can apply the procedure outlined in Appendix A of Hill et al. (2017) to compute a barotropic adjustment, \mathbf{v}_{adj} , to the horizontal winds such that the budget in Equation A2 is closed. The adjusted horizontal winds are thus:

$$\mathbf{v} = \mathbf{v}_{\text{raw}} - \mathbf{v}_{\text{adj}},\tag{A3}$$

where \mathbf{v}_{raw} are the raw horizontal winds output on model-native vertical levels. Using the adjusted winds to compute the horizontal advection term in Equation A1 explicitly, we can then compute the vertical advection term as a residual:

$$-\left\{\omega \frac{\partial s}{\partial p}\right\} = \frac{\partial \left\{s\right\}}{\partial t} + \left\{\mathbf{v} \cdot \nabla s\right\} - P - F - H,\tag{A4}$$

where the terms on the right hand side are all computed explicitly. Note that this is the same vertical advection term as in internal energy budget, Equation 12. Accordingly, we can use the adjusted winds derived here to compute the horizontal temperature advection terms in Equation 12:

$$C_{p} \frac{\partial \left\{T\right\}'}{\partial t} = -C_{p} \left\{\mathbf{v} \cdot \nabla T\right\}' - \left\{\omega \frac{\partial s}{\partial p}\right\}' + P' + F' + H'. \tag{A5}$$

Because we compute the vertical advection term as a residual from the dry static energy budget,
when we plug it back in to the internal energy equation, Equation A5, we have a small residual,
shown in Figure 11(d).

876 References

Adames, Á. F., and D. Kim, 2015: The MJO as a Dispersive, Convectively Coupled Moisture
Wave: Theory and Observations. *Journal of the Atmospheric Sciences*, **73** (**3**), 913–941, doi:
10.1175/JAS-D-15-0170.1.

Adames, Á. F., and Y. Ming, 2018a: Interactions between Water Vapor and Potential Vorticity
in Synoptic-Scale Monsoonal Disturbances: Moisture Vortex Instability. *Journal of the Atmo-*spheric Sciences, **75** (6), 2083–2106, doi:10.1175/JAS-D-17-0310.1.

Adames, Á. F., and Y. Ming, 2018b: Moisture and moist static energy budgets of South Asian monsoon low pressure systems in GFDL AM4.0. *Journal of the Atmospheric Sciences*, doi: 10.1175/JAS-D-17-0309.1.

- Adames, Á. F., and J. M. Wallace, 2014: Three-Dimensional Structure and Evolution of the MJO and Its Relation to the Mean Flow. *Journal of the Atmospheric Sciences*, **71** (**6**), 2007–2026,
- doi:10.1175/JAS-D-13-0254.1.
- Ajayamohan, R. S., B. Khouider, and A. J. Majda, 2014: Simulation of monsoon intraseasonal oscillations in a coarse-resolution aquaplanet GCM. *Geophysical Research Letters*, **41** (**15**),
- 5662–5669, doi:10.1002/2014GL060662.
- Ajayamohan, R. S., W. J. Merryfield, and V. V. Kharin, 2010: Increasing Trend of Synoptic Ac-
- tivity and Its Relationship with Extreme Rain Events over Central India. *Journal of Climate*,
- 23 (4), 1004–1013, doi:10.1175/2009JCLI2918.1.
- Andersen, J. A., and Z. Kuang, 2011: Moist Static Energy Budget of MJO-like Disturbances in
- the Atmosphere of a Zonally Symmetric Aquaplanet. *Journal of Climate*, **25** (8), 2782–2804,
- doi:10.1175/JCLI-D-11-00168.1.
- Becker, T., and B. Stevens, 2014: Climate and climate sensitivity to changing CO2 on an idealized
- land planet. Journal of Advances in Modeling Earth Systems, 6 (4), 1205–1223, doi:10.1002/
- ⁹⁰⁰ 2014MS000369.
- Blackburn, M., and Coauthors, 2013: The Aqua-Planet Experiment (APE): CONTROL SST Sim-
- ulation. Journal of the Meteorological Society of Japan. Ser. II, 91A, 17–56, doi:10.2151/jmsj.
- 903 2013-A02.
- Boos, W. R., J. V. Hurley, and V. S. Murthy, 2015: Adiabatic westward drift of Indian monsoon
- depressions. Quarterly Journal of the Royal Meteorological Society, 141 (689), 1035–1048,
- good doi:10.1002/qj.2454.

- Boos, W. R., and R. L. Korty, 2016: Regional energy budget control of the intertropical convergence zone and application to mid-Holocene rainfall. *Nature Geoscience*, **9** (**12**), 892–897, doi:10.1038/ngeo2833.
- Boville, B. A., 1986: Wave–Mean Flow Interactions in a General Circulation Model of the Troposphere and Stratosphere. *Journal of the Atmospheric Sciences*, **43** (**16**), 1711–1725, doi:
 10.1175/1520-0469(1986)043\(\frac{1711:WFIIAG}{2.0.CO};2.
- Bretherton, C. S., M. E. Peters, and L. E. Back, 2004: Relationships between Water Vapor Path and Precipitation over the Tropical Oceans. *Journal of Climate*, **17** (7), 1517–1528, doi:10.1175/
- Byrne, M. P., and P. A. O'Gorman, 2012: Land–Ocean Warming Contrast over a Wide Range of
 Climates: Convective Quasi-Equilibrium Theory and Idealized Simulations. *Journal of Climate*,
 26 (12), 4000–4016, doi:10.1175/JCLI-D-12-00262.1.
- Clark, S. K., Y. Ming, I. M. Held, and P. J. Phillipps, 2018: The Role of the Water Vapor Feedback in the ITCZ Response to Hemispherically Asymmetric Forcings. *Journal of Climate*, **31** (9), 3659–3678, doi:10.1175/JCLI-D-17-0723.1.
- Cohen, N. Y., and W. R. Boos, 2016: Perspectives on Moist Baroclinic Instability: Implications for the Growth of Monsoon Depressions. *Journal of the Atmospheric Sciences*, **73** (4), 1767–1788, doi:10.1175/JAS-D-15-0254.1.
- Collins, N., and Coauthors, 2005: Design and Implementation of Components in the Earth System
 Modeling Framework. *The International Journal of High Performance Computing Applications*,
 19 (3), 341–350, doi:10.1177/1094342005056120.

Cronin, T. W., K. A. Emanuel, and P. Molnar, 2015: Island precipitation enhancement and the di-928 urnal cycle in radiative-convective equilibrium. Quarterly Journal of the Royal Meteorological 929 Society, **141** (**689**), 1017–1034, doi:10.1002/qj.2443.

- Dee, D. P., and Coauthors, 2011: The ERA-Interim reanalysis: Configuration and performance of 931 the data assimilation system. Quarterly Journal of the Royal Meteorological Society, 137 (656), 932 553–597, doi:10.1002/qj.828.
- Diaz, M., and W. R. Boos, 2019: Barotropic growth of monsoon depressions. Quarterly Journal of the Royal Meteorological Society, **145** (**719**), 824–844, doi:10.1002/qj.3467. 935
- Ditchek, S. D., W. R. Boos, S. J. Camargo, and M. K. Tippett, 2016: A Genesis Index for Monsoon 936 Disturbances. Journal of Climate, 29 (14), 5189–5203, doi:10.1175/JCLI-D-15-0704.1. 937
- Emanuel, K. A., M. Fantini, and A. J. Thorpe, 1987: Baroclinic Instability in an Environment of 938 Small Stability to Slantwise Moist Convection. Part I: Two-Dimensional Models. *Journal of the* Atmospheric Sciences, 44 (12), 1559–1573, doi:10.1175/1520-0469(1987)044 \langle 1559:BIIAEO \rangle 940 2.0.CO;2. 941
- Frierson, D. M. W., 2007a: Convectively Coupled Kelvin Waves in an Idealized Moist General Circulation Model. Journal of the Atmospheric Sciences, 64 (6), 2076–2090, doi:10.1175/JAS3945. 1. 944
- Frierson, D. M. W., 2007b: The Dynamics of Idealized Convection Schemes and Their Effect 945 on the Zonally Averaged Tropical Circulation. Journal of the Atmospheric Sciences, 64 (6), 946 1959–1976, doi:10.1175/JAS3935.1.

- Frierson, D. M. W., I. M. Held, and P. Zurita-Gotor, 2006: A Gray-Radiation Aquaplanet Moist
- GCM. Part I: Static Stability and Eddy Scale. Journal of the Atmospheric Sciences, 63 (10),
- 2548–2566, doi:10.1175/JAS3753.1.
- 951 Frierson, D. M. W., I. M. Held, and P. Zurita-Gotor, 2007: A Gray-Radiation Aquaplanet Moist
- 952 GCM. Part II: Energy Transports in Altered Climates. Journal of the Atmospheric Sciences,
- 953 **64 (5)**, 1680–1693, doi:10.1175/JAS3913.1.
- Gates, W. L., 1992: AMIP: The Atmospheric Model Intercomparison Project. Bulletin of the Amer-
- ican Meteorological Society, **73** (**12**), 1962–1970, doi:10.1175/1520-0477(1992)073(1962:
- $ATAMIP \ge 2.0.CO; 2.$
- Geen, R., F. H. Lambert, and G. K. Vallis, 2017: Regime Change Behavior during Asian Monsoon
- Onset. Journal of Climate, **31 (8)**, 3327–3348, doi:10.1175/JCLI-D-17-0118.1.
- Godbole, R. V., 1977: The composite structure of the monsoon depression. *Tellus*, **29** (1), 25–40,
- doi:10.1111/j.2153-3490.1977.tb00706.x.
- Haertel, P. T., G. N. Kiladis, A. Denno, and T. M. Rickenbach, 2008: Vertical-Mode Decomposi-
- tions of 2-Day Waves and the Madden–Julian Oscillation. *Journal of the Atmospheric Sciences*,
- 963 **65 (3)**, 813–833, doi:10.1175/2007JAS2314.1.
- Hendon, H. H., and M. C. Wheeler, 2008: Some Space-Time Spectral Analyses of Tropical Con-
- vection and Planetary-Scale Waves. *Journal of the Atmospheric Sciences*, **65** (9), 2936–2948,
- 966 doi:10.1175/2008JAS2675.1.
- 967 Hill, S. A., Y. Ming, I. M. Held, and M. Zhao, 2017: A Moist Static Energy Budget–Based
- Analysis of the Sahel Rainfall Response to Uniform Oceanic Warming. *Journal of Climate*,
- **30** (**15**), 5637–5660, doi:10.1175/JCLI-D-16-0785.1.

- 970 Huffman, G. J., and Coauthors, 2007: The TRMM Multisatellite Precipitation Analysis (TMPA):
- ⁹⁷¹ Quasi-Global, Multiyear, Combined-Sensor Precipitation Estimates at Fine Scales. *Journal of*
- 972 *Hydrometeorology*, **8** (**1**), 38–55, doi:10.1175/JHM560.1.
- Hunt, K. M., and A. G. Turner, 2017: The effect of horizontal resolution on Indian monsoon de-
- pressions in the Met Office NWP model. Quarterly Journal of the Royal Meteorological Society,
- 975 **143 (705)**, 1756–1771, doi:10.1002/qj.3030.
- 976 Hunt, K. M. R., and J. K. Fletcher, 2019: The relationship between Indian monsoon
- rainfall and low-pressure systems. Climate Dynamics, 53 (3), 1859–1871, doi:10.1007/
- 978 s00382-019-04744-x.
- Hunt, K. M. R., and D. J. Parker, 2016: The movement of Indian monsoon depressions by interac-
- tion with image vortices near the Himalayan wall. Quarterly Journal of the Royal Meteorologi-
- cal Society, **142** (**698**), 2224–2229, doi:10.1002/qj.2812.
- Hunt, K. M. R., A. G. Turner, P. M. Inness, D. E. Parker, and R. C. Levine, 2016a: On the Structure
- and Dynamics of Indian Monsoon Depressions. *Monthly Weather Review*, **144** (9), 3391–3416,
- doi:10.1175/MWR-D-15-0138.1.
- Hunt, K. M. R., A. G. Turner, and D. E. Parker, 2016b: The spatiotemporal structure of precipi-
- tation in Indian monsoon depressions. Quarterly Journal of the Royal Meteorological Society,
- 987 **142 (701)**, 3195–3210, doi:10.1002/qj.2901.
- Hurley, J. V., and W. R. Boos, 2015: A global climatology of monsoon low-pressure systems.
- Quarterly Journal of the Royal Meteorological Society, **141** (689), 1049–1064, doi:10.1002/qj.
- 990 2447.

- Jablonowski, C., and D. L. Williamson, 2011: The Pros and Cons of Diffusion, Filters and Fixers in Atmospheric General Circulation Models. *Numerical Techniques for Global Atmospheric Models*, P. Lauritzen, C. Jablonowski, M. Taylor, and R. Nair, Eds., Lecture Notes in Computational Science and Engineering, Springer Berlin Heidelberg, Berlin, Heidelberg, 381–493, doi:10.1007/978-3-642-11640-7_13.
- Jucker, M., and E. P. Gerber, 2017: Untangling the Annual Cycle of the Tropical Tropopause

 Layer with an Idealized Moist Model. *Journal of Climate*, **30** (**18**), 7339–7358, doi:10.1175/

 JCLI-D-17-0127.1.
- Kiladis, G. N., M. C. Wheeler, P. T. Haertel, K. H. Straub, and P. E. Roundy, 2009: Convectively coupled equatorial waves. *Reviews of Geophysics*, **47** (2), doi:10.1029/2008RG000266.
- Kim, D., J.-S. Kug, and A. H. Sobel, 2013: Propagating versus Nonpropagating Madden–Julian
 Oscillation Events. *Journal of Climate*, **27** (1), 111–125, doi:10.1175/JCLI-D-13-00084.1.
- Krishnamurti, T. N., M. Kanamitsu, R. Godbole, C.-B. Chang, F. Carr, and J. H. Chow, 1976:

 Study of a Monsoon Depression (II), Dynamical Structure. *Journal of the Meteorological Society of Japan. Ser. II*, **54** (**4**), 208–225, doi:10.2151/jmsj1965.54.4_208.
- Krishnamurti, T. N., A. Martin, R. Krishnamurti, A. Simon, A. Thomas, and V. Kumar, 2013: Impacts of enhanced CCN on the organization of convection and recent reduced counts of monsoon depressions. *Climate Dynamics*, **41** (1), 117–134, doi:10.1007/s00382-012-1638-z.
- Lindberg, C., and A. J. Broccoli, 1996: Representation of Topography in Spectral Climate Models and Its Effect on Simulated Precipitation. *Journal of Climate*, **9** (**11**), 2641–2659, doi:10.1175/

- Lindzen, R. S., B. Farrell, and A. J. Rosenthal, 1983: Absolute Barotropic Instability and Monsoon Depressions. *Journal of the Atmospheric Sciences*, **40** (**5**), 1178–1184, doi:10.1175/
- Lutsko, N. J., 2017: The Response of an Idealized Atmosphere to Localized Tropical Heating:

 Superrotation and the Breakdown of Linear Theory. *Journal of the Atmospheric Sciences*, **75** (1),

 3–20, doi:10.1175/JAS-D-17-0192.1.
- Mak, M., 1983: A Moist Baroclinic Model for Monsoonal Mid-Tropospheric Cyclogenesis. *Journal of the Atmospheric Sciences*, **40** (**5**), 1154–1162, doi:10.1175/1520-0469(1983)040⟨1154:
 AMBMFM⟩2.0.CO;2.
- Manabe, S., 1969: Climate and the ocean circulation. *Monthly Weather Review*, **97** (**11**), 739–774, doi:10.1175/1520-0493(1969)097(0739:CATOC)2.3.CO;2.
- Maroon, E. A., and D. M. W. Frierson, 2016: The impact of a continent's longitudinal extent on tropical precipitation. *Geophysical Research Letters*, **43** (**22**), 11,921–11,929, doi:10.1002/ 2016GL071518.
- Maroon, E. A., D. M. W. Frierson, S. M. Kang, and J. Scheff, 2016: The Precipitation Response to an Idealized Subtropical Continent. *Journal of Climate*, **29** (**12**), 4543–4564, doi:10.1175/

 JCLI-D-15-0616.1.
- Masunaga, H., T. S. L'Ecuyer, and C. D. Kummerow, 2006: The Madden–Julian Oscillation

 Recorded in Early Observations from the Tropical Rainfall Measuring Mission (TRMM). *Jour-*nal of the Atmospheric Sciences, **63** (**11**), 2777–2794, doi:10.1175/JAS3783.1.

- Merlis, T. M., T. Schneider, S. Bordoni, and I. Eisenman, 2012a: Hadley Circulation Response to Orbital Precession. Part I: Aquaplanets. *Journal of Climate*, **26** (3), 740–753, doi:10.1175/

 JCLI-D-11-00716.1.
- Merlis, T. M., T. Schneider, S. Bordoni, and I. Eisenman, 2012b: Hadley Circulation Response to Orbital Precession. Part II: Subtropical Continent. *Journal of Climate*, **26** (**3**), 754–771, doi: 10.1175/JCLI-D-12-00149.1.
- Mishra, S. K., and P. S. Salvekar, 1980: Role of Baroclinic Instability in the Development of

 Monsoon Disturbances. *Journal of the Atmospheric Sciences*, **37** (2), 383–394, doi:10.1175/

 1520-0469(1980)037\(0383:ROBIIT\)2.0.CO;2.
- Moorthi, S., and A. Arakawa, 1985: Baroclinic Instability with Cumulus Heating. *Journal of the*Atmospheric Sciences, **42** (**19**), 2007–2031, doi:10.1175/1520-0469(1985)042\(2007:BIWCH\)

 2.0.CO;2.
- Muller, C. J., and D. M. Romps, 2018: Acceleration of tropical cyclogenesis by self-aggregation feedbacks. *Proceedings of the National Academy of Sciences*, **115** (**12**), 2930–2935, doi:10. 1073/pnas.1719967115.
- Neelin, J. D., 2007: Moist dynamics of tropical convection zones in monsoons, teleconnections and global warming. *The Global Circulation of the Atmosphere*, Princeton University Press, 267–302.
- Neelin, J. D., and N. Zeng, 2000: A Quasi-Equilibrium Tropical Circulation Model—Formulation. *Journal of the Atmospheric Sciences*, **57** (**11**), 1741–1766, doi:10.1175/1520-0469(2000)

 057\(\frac{1741}{1741}\):AQETCM\(\frac{2}{300}\):2.0.CO;2.

- O'Gorman, P. A., and T. Schneider, 2008: The Hydrological Cycle over a Wide Range of
 Climates Simulated with an Idealized GCM. *Journal of Climate*, **21** (**15**), 3815–3832, doi:
 10.1175/2007JCLI2065.1.
- Praveen, V., S. Sandeep, and R. S. Ajayamohan, 2015: On the Relationship between Mean Monsoon Precipitation and Low Pressure Systems in Climate Model Simulations. *Journal of Cli-*mate, **28** (**13**), 5305–5324, doi:10.1175/JCLI-D-14-00415.1.
- Sandeep, S., R. S. Ajayamohan, W. R. Boos, T. P. Sabin, and V. Praveen, 2018: Decline and poleward shift in Indian summer monsoon synoptic activity in a warming climate. *Proceedings*of the National Academy of Sciences, 115 (11), 2681–2686, doi:10.1073/pnas.1709031115.
- Seager, R., and N. Henderson, 2013: Diagnostic Computation of Moisture Budgets in the ERAInterim Reanalysis with Reference to Analysis of CMIP-Archived Atmospheric Model Data. *Journal of Climate*, **26** (**20**), 7876–7901, doi:10.1175/JCLI-D-13-00018.1.
- Shukla, J., 1977: Barotropic-Baroclinic instability of mean zonal wind during summer monsoon.

 Pure and Applied Geophysics, **115** (**5-6**), 1449–1461, doi:10.1007/BF00874418.
- Shukla, J., 1978: CISK-Barotropic-Baroclinic Instability and the Growth of Monsoon Depressions. *Journal of the Atmospheric Sciences*, **35** (3), 495–508, doi:10.1175/1520-0469(1978) $035\langle0495:CBBIAT\rangle2.0.CO;2.$
- Sikka, D. R., 1977: Some aspects of the life history, structure and movement of monsoon depressions. *Pure and Applied Geophysics*, **115** (**5-6**), 1501–1529, doi:10.1007/BF00874421.
- Tamarin, T., and Y. Kaspi, 2016: The Poleward Motion of Extratropical Cyclones from a Potential Vorticity Tendency Analysis. *Journal of the Atmospheric Sciences*, **73** (**4**), 1687–1707, doi: 10.1175/JAS-D-15-0168.1.

- Taylor, K. E., R. J. Stouffer, and G. A. Meehl, 2012: An Overview of CMIP5 and the Experiment Design. *Bulletin of the American Meteorological Society*, **93** (**4**), 485–498, doi: 10.1175/BAMS-D-11-00094.1.
- Vallis, G. K., 2006: *Atmospheric and Oceanic Fluid Dynamics*. Cambridge University Press, The
 Edinburgh Building, Cambridge CB2 8RU, UK.
- Vallis, G. K., and Coauthors, 2018: Isca, v1.0: A framework for the global modelling of the atmospheres of Earth and other planets at varying levels of complexity. *Geoscientific Model Development*, **11** (3), 843–859, doi:10.5194/gmd-11-843-2018.
- Voigt, A., and Coauthors, 2016: The tropical rain belts with an annual cycle and a continent model intercomparison project: TRACMIP. *Journal of Advances in Modeling Earth Systems*, n/a–n/a, doi:10.1002/2016MS000748.
- Welch, P., 1967: The use of fast Fourier transform for the estimation of power spectra: A method based on time averaging over short, modified periodograms. *IEEE Transactions on Audio and Electroacoustics*, **15** (2), 70–73, doi:10.1109/TAU.1967.1161901.
- Wheeler, M., and G. N. Kiladis, 1999: Convectively Coupled Equatorial Waves: Analysis of Clouds and Temperature in the Wavenumber–Frequency Domain. *Journal of the Atmospheric*Sciences, **56** (3), 374–399, doi:10.1175/1520-0469(1999)056(0374:CCEWAO)2.0.CO;2.
- Xie, S.-P., and N. Saiki, 1999: Abrupt Onset and Slow Seasonal Evolution of Summer Monsoon in an Idealized GCM Simulation. *Journal of the Meteorological Society of Japan. Ser. II*, **77** (4), 949–968, doi:https://doi.org/10.2151/jmsj1965.77.4_949.
- Zhou, W., and S.-P. Xie, 2018: A Hierarchy of Idealized Monsoons in an Intermediate GCM. *Journal of Climate*, **31** (**22**), 9021–9036, doi:10.1175/JCLI-D-18-0084.1.

Zhuang, J., and A. Jüling, 2019: JiaweiZhuang/xESMF: V0.2.0: Dask and Dataset support. Zenodo, doi:10.5281/zenodo.3360047.

1099 LIST OF FIGURES

1100 1101 1102 1103 1104 1105	Fig. 1.	JJAS-mean precipitation rate (a) and (b); JJAS-mean column-integrated water vapor (c) and (d); and JJAS-mean temperature at 600 hPa (colors) (e) and (f). Vectors in (e) and (f) represent the direction and magnitude of the difference in horizontal wind between 200 hPa and 850 hPa (i.e. upper level winds minus lower level winds). The columns represent data from observations, in this case TRMM (Huffman et al. 2007) and ERA-Interim reanalysis (Dee et al. 2011), and the simulation, respectively. Note the differences in the colorbar scales for each column.	. 56
1107 1108 1109 1110 1111	Fig. 2.	Time-longitude diagram of unfiltered (colors) and filtered (contours) precipitation rate over the South Asian monsoon region during JJAS of year 0016 in the idealized simulation. Solid contour lines represent filtered anomalous precipitation rates of $1.5 \mathrm{mm} \mathrm{d}^{-1}$ and dashed contour lines represent filtered anomalous precipitation rates of $-1.5 \mathrm{mm} \mathrm{d}^{-1}$. Precipitation is filtered to isolate precipitation anomalies due to MLPS-like disturbances using the spectral filtering procedure described in Section $2.c2$. 57
1113 1114 1115	Fig. 3.	Frequency-wavenumber spectrum of the JJAS precipitation rate in TRMM (Huffman et al. 2007) observations (a) and the simulation (b). All values below the 99% threshold for statistical significance (0.33 for the observations, 0.38 for the simulation) are masked	. 58
1116 1117 1118 1119 1120 1121 1122	Fig. 4.	Precipitation rate (colors), pressure velocity at $500\mathrm{hPa}$ (contour lines), and $850\mathrm{hPa}$ horizontal winds (arrows) lag-regressed onto the precipitation index defined in Section 2c for the idealized simulation. Only precipitation anomalies statistically significant at the 99% level are plotted. Contour levels for the vertical velocity anomalies begin at $-0.0375\mathrm{Pas}^{-1}$ and are evenly spaced by $0.015\mathrm{Pa}\mathrm{s}^{-1}$; negative contours are dashed, while positive contours are solid. The lag day is indicated in the upper right portion of each row (time moves forward downward). In all panels, the maximum of the vorticity anomalies at $850\mathrm{hPa}$ is indicated by the filled black dot	. 59
1124 1125 1126 1127 1128 1129 1130	Fig. 5.	Zonal cross section of EPV (colors) and temperature (lines) anomalies in the idealized experiment (a); Meridional cross section of EPV anomalies (colors) and JJAS mean zonal wind (lines) (b). Only statistically significant anomalies at the 99% level are shown. The dashed contours represent negative values, while the solid contours represent positive values. In (b) the bold contour is the zero line. The first temperature anomaly contour in (a) greater than (less than) zero is $0.075 \text{K} (-0.075 \text{K})$; with the exception of the omission of the zero contour, temperature anomaly contours are separated by 0.075K . The zonal wind contours in (b) are separated by 2ms^{-1}	. 60
1132 1133 1134 1135	Fig. 6.	Anomalous terms in the EPV budget in the idealized simulation at 500 hPa (row one) and 700 hPa (row two). The solid black contours represent isolines of EPV anomalies of 0.01 PVU and 0.02 PVU, while the dashed black contours represent isolines of PV of -0.01 PVU. Only values statistically significant at the 99% level are shown	. 61
1136 1137 1138	Fig. 7.	Projection of EPV budget terms on $\frac{\partial q'_d}{\partial t}$ in the idealized simulation. The sum of the colored lines results in the black dashed line; if numerical errors are small, it should stay close to a value of one.	62
1139 1140 1141 1142	Fig. 8.	Projection of terms comprising the total horizontal advection anomaly (see Equation 10) on $\frac{\partial q'_d}{\partial t}$ in the idealized simulation. The sum of the red and blue lines results in the yellow line, the projection of the total anomalous horizontal advection term, $-(\mathbf{v} \cdot \nabla q_d)'$, onto the total anomalous time tendency of PV.	. 63

1143 1144 1145 1146 1147	Fig. 9.	Terms in the anomalous vorticity budget (colors) at 400 hPa (row one) and 850 hPa (row two). Only values statistically significant at the 99% level are shown. Contours represent relative vorticity anomalies, ζ' ; contour levels start at $\pm 1.0 \times 10^{-6} \mathrm{s}^{-1}$ and are separated by intervals of $2.0 \times 10^{-6} \mathrm{s}^{-1}$. Dashed contours represent negative anomalies, while solid contours represent positive anomalies.	64
1148	Fig. 10.	Projection of vorticity budget terms on the time tendency of the relative vorticity	65
1149 1150 1151 1152 1153	Fig. 11.	Terms in the anomalous internal energy budget (colors) with anomalous column-integrated internal energy, $C_p\{T\}'$, overlaid (contours). Only budget values statistically significant at a 99% level are shown. Negative contours are dashed; positive contours are solid. With the exception of the omission of the zero contour, contours are separated by an interval of $2.5 \times 10^5 \mathrm{Jkg}^{-1}$.	66
1154 1155 1156 1157	Fig. 12.	Projection of the terms on the right hand side of the column-integrated internal energy budget sorted in descending order by absolute value. The horizontal advection term is comprehensively decomposed into linear and nonlinear components. The sum of the components adds exactly to 1.0.	67
1158 1159 1160 1161 1162	Fig. 13.	Terms in the anomalous moisture budget (colors). Only tendency anomalies statistically significant at the 99% level are shown. Contours represent column-integrated moisture anomalies scaled by the latent heat of vaporization, L_{ν} . Negative contours are dashed; positive contours are solid. With the exception of the omission of the zero contour, contours are separated by intervals of $4.0 \times 10^5 \mathrm{J} \mathrm{m}^{-2}$	68
1163 1164 1165	Fig. 14.	Projection of the terms on the right hand side of the column-integrated moisture budget sorted in descending order by absolute value. The horizontal advection term is comprehensively decomposed into linear and nonlinear components. The sum of the components adds exactly to 1.0	69

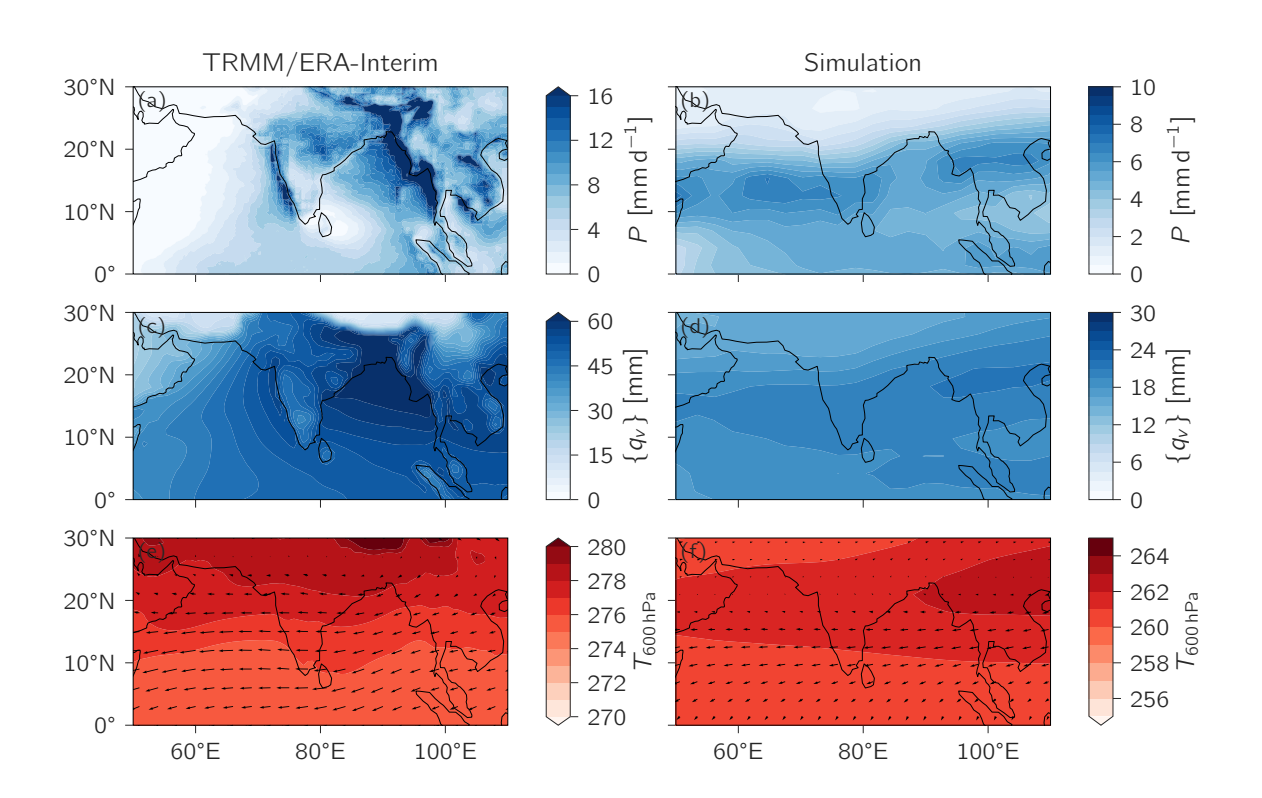


FIG. 1. JJAS-mean precipitation rate (a) and (b); JJAS-mean column-integrated water vapor (c) and (d); and JJAS-mean temperature at 600 hPa (colors) (e) and (f). Vectors in (e) and (f) represent the direction and magnitude of the difference in horizontal wind between 200 hPa and 850 hPa (i.e. upper level winds minus lower level winds). The columns represent data from observations, in this case TRMM (Huffman et al. 2007) and ERA-Interim reanalysis (Dee et al. 2011), and the simulation, respectively. Note the differences in the colorbar scales for each column.

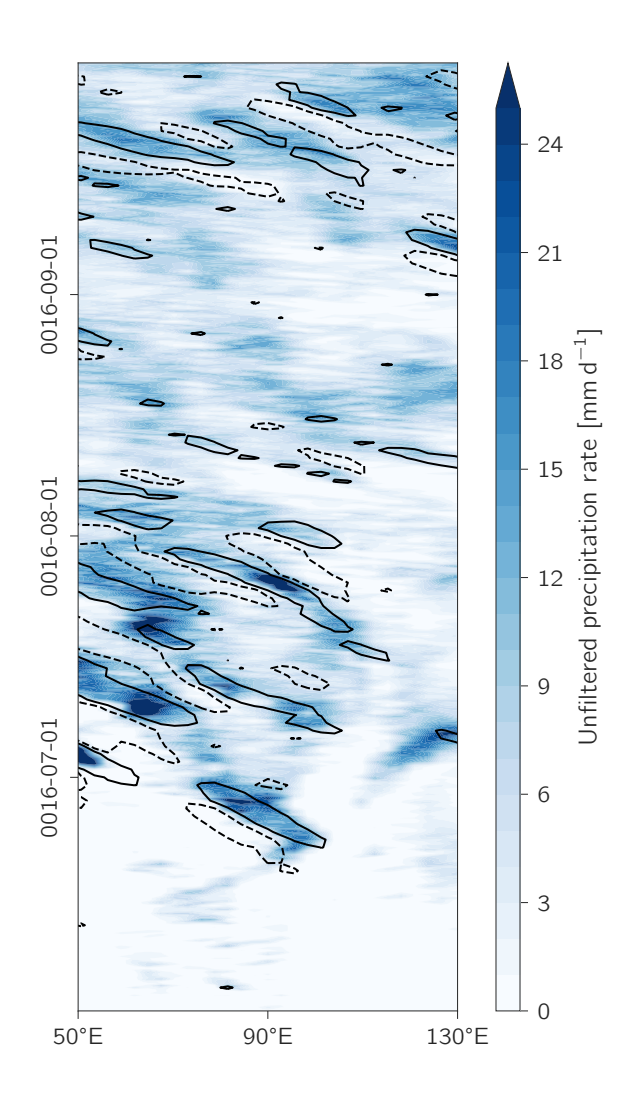


Fig. 2. Time-longitude diagram of unfiltered (colors) and filtered (contours) precipitation rate over the South Asian monsoon region during JJAS of year 0016 in the idealized simulation. Solid contour lines represent filtered anomalous precipitation rates of $1.5 \text{ mm} \text{ d}^{-1}$ and dashed contour lines represent filtered anomalous precipitation rates of $-1.5 \text{ mm} \text{ d}^{-1}$. Precipitation is filtered to isolate precipitation anomalies due to MLPS-like disturbances using the spectral filtering procedure described in Section 2.c2.

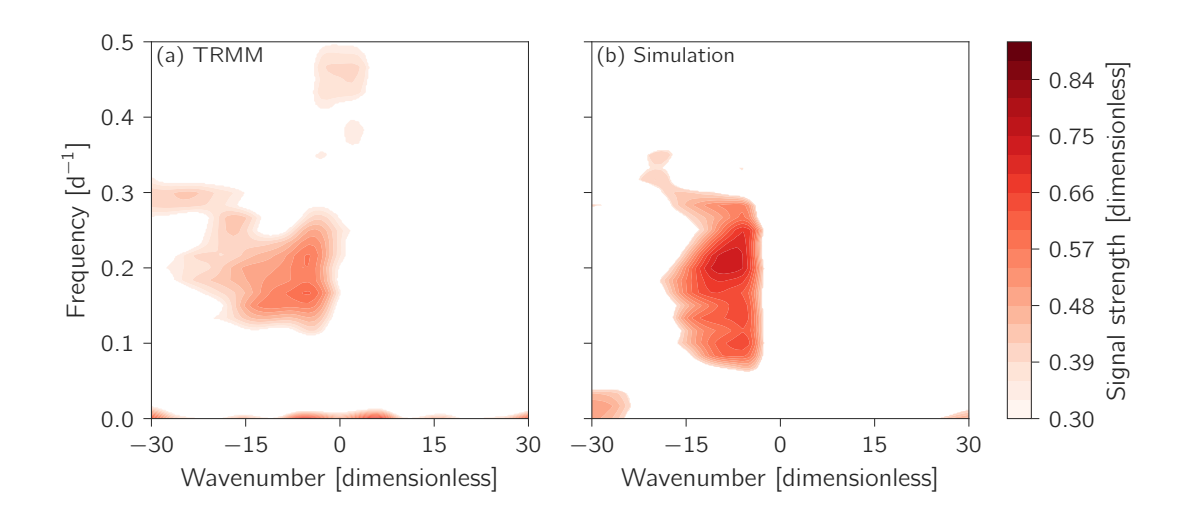


FIG. 3. Frequency-wavenumber spectrum of the JJAS precipitation rate in TRMM (Huffman et al. 2007) observations (a) and the simulation (b). All values below the 99% threshold for statistical significance (0.33 for the observations, 0.38 for the simulation) are masked.

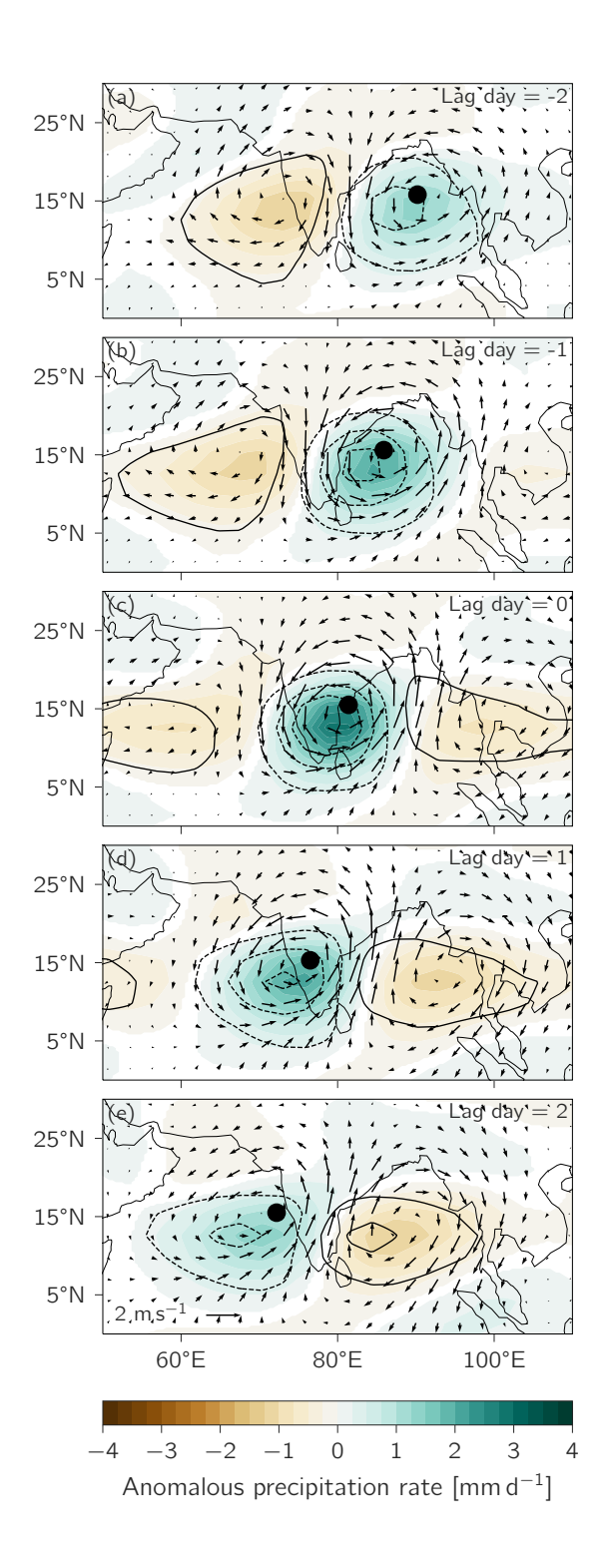


FIG. 4. Precipitation rate (colors), pressure velocity at 500 hPa (contour lines), and 850 hPa horizontal winds (arrows) lag-regressed onto the precipitation index defined in Section 2c for the idealized simulation. Only precipitation anomalies statistically significant at the 99% level are plotted. Contour levels for the vertical velocity anomalies begin at $-0.0375 \, \mathrm{Pa} \, \mathrm{s}^{-1}$ and are evenly spaced by $0.015 \, \mathrm{Pa} \, \mathrm{s}^{-1}$; negative contours are dashed, while positive contours are solid. The lag day is indicated in the upper right portion of each row (time moves forward downward). In all panels, the maximum of the vorticity anomalies at 850 hPa is indicated by the filled black dot.

Accepted for publication in Journal of Climate. DOI10.1175/JCLI-D-19-0289.1.

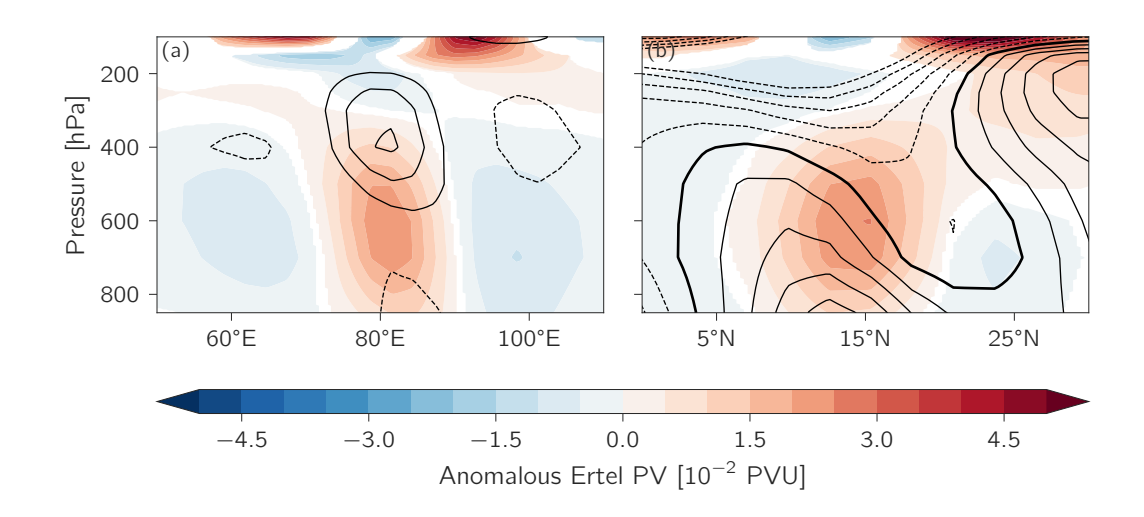


FIG. 5. Zonal cross section of EPV (colors) and temperature (lines) anomalies in the idealized experiment (a); Meridional cross section of EPV anomalies (colors) and JJAS mean zonal wind (lines) (b). Only statistically significant anomalies at the 99% level are shown. The dashed contours represent negative values, while the solid contours represent positive values. In (b) the bold contour is the zero line. The first temperature anomaly contour in (a) greater than (less than) zero is $0.075 \, \text{K}$ ($-0.075 \, \text{K}$); with the exception of the omission of the zero contour, temperature anomaly contours are separated by $0.075 \, \text{K}$. The zonal wind contours in (b) are separated by $2 \, \text{ms}^{-1}$.

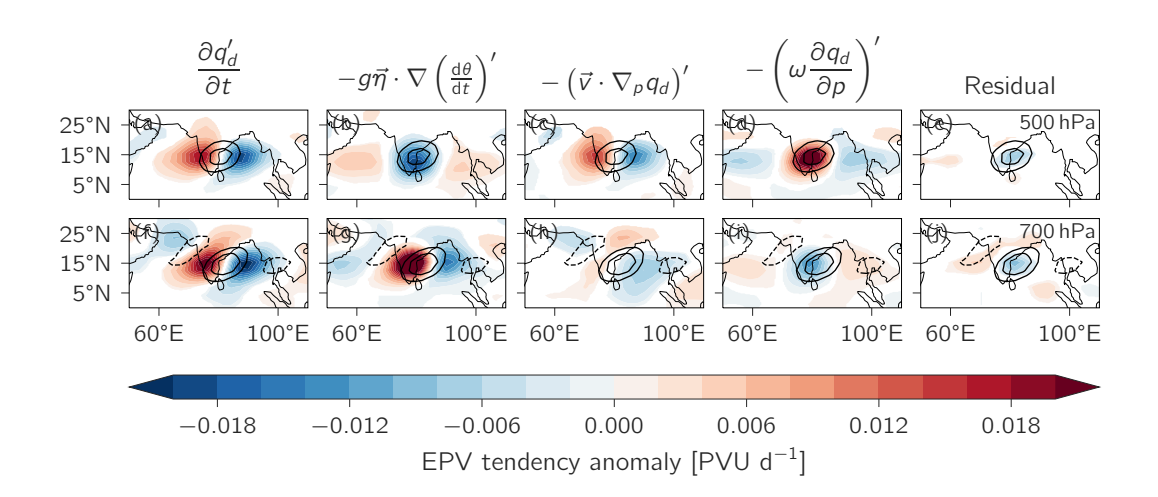


FIG. 6. Anomalous terms in the EPV budget in the idealized simulation at $500 \,\mathrm{hPa}$ (row one) and $700 \,\mathrm{hPa}$ (row two). The solid black contours represent isolines of EPV anomalies of $0.01 \,\mathrm{PVU}$ and $0.02 \,\mathrm{PVU}$, while the dashed black contours represent isolines of PV of $-0.01 \,\mathrm{PVU}$. Only values statistically significant at the 99% level are shown.

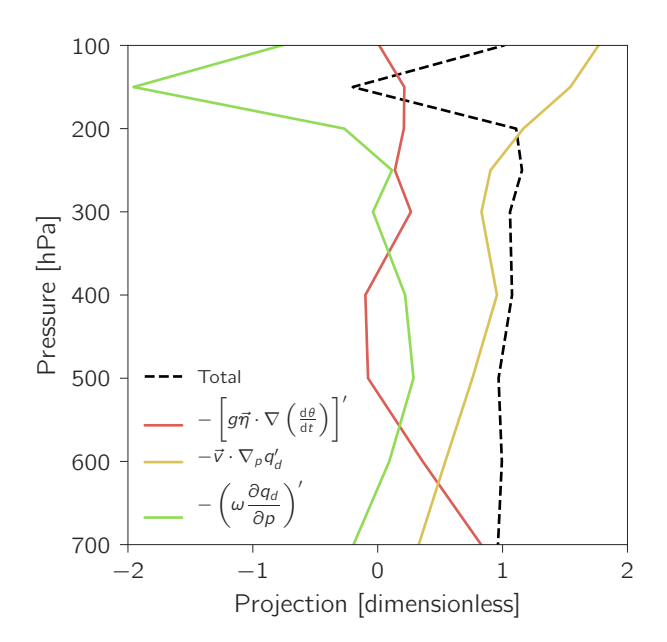


FIG. 7. Projection of EPV budget terms on $\frac{\partial q'_d}{\partial t}$ in the idealized simulation. The sum of the colored lines results in the black dashed line; if numerical errors are small, it should stay close to a value of one.

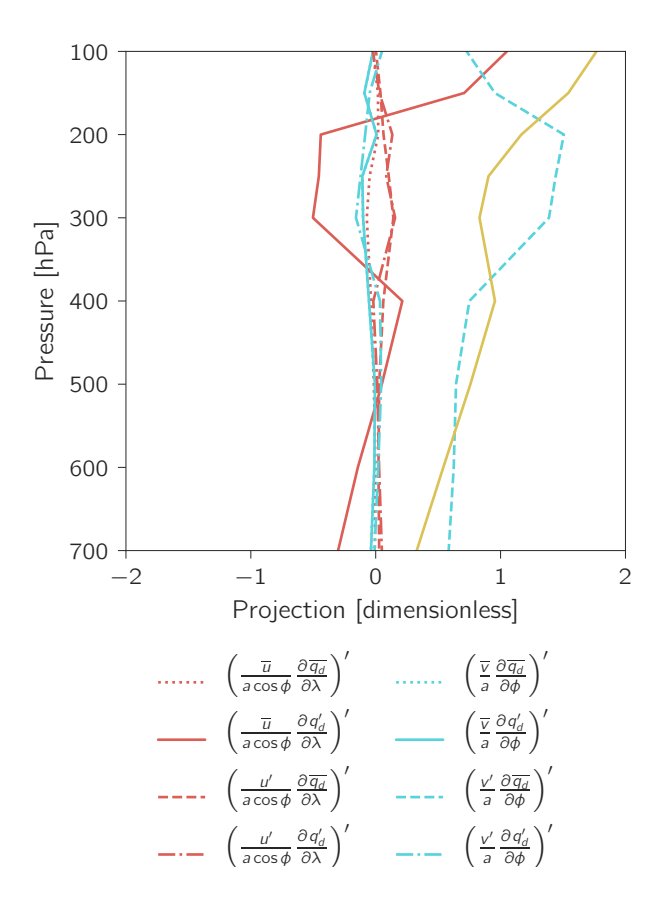


FIG. 8. Projection of terms comprising the total horizontal advection anomaly (see Equation 10) on $\frac{\partial q'_d}{\partial t}$ in the idealized simulation. The sum of the red and blue lines results in the yellow line, the projection of the total anomalous horizontal advection term, $-(\mathbf{v} \cdot \nabla q_d)'$, onto the total anomalous time tendency of PV.

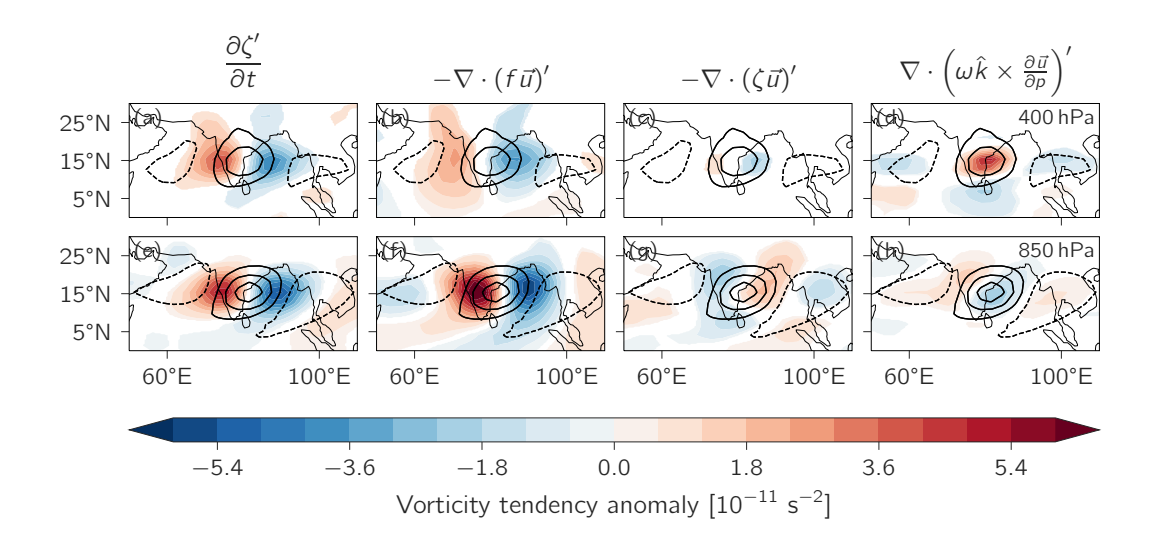


FIG. 9. Terms in the anomalous vorticity budget (colors) at 400 hPa (row one) and 850 hPa (row two). Only values statistically significant at the 99% level are shown. Contours represent relative vorticity anomalies, ζ' ; contour levels start at $\pm 1.0 \times 10^{-6}$ s⁻¹ and are separated by intervals of 2.0×10^{-6} s⁻¹. Dashed contours represent negative anomalies, while solid contours represent positive anomalies.

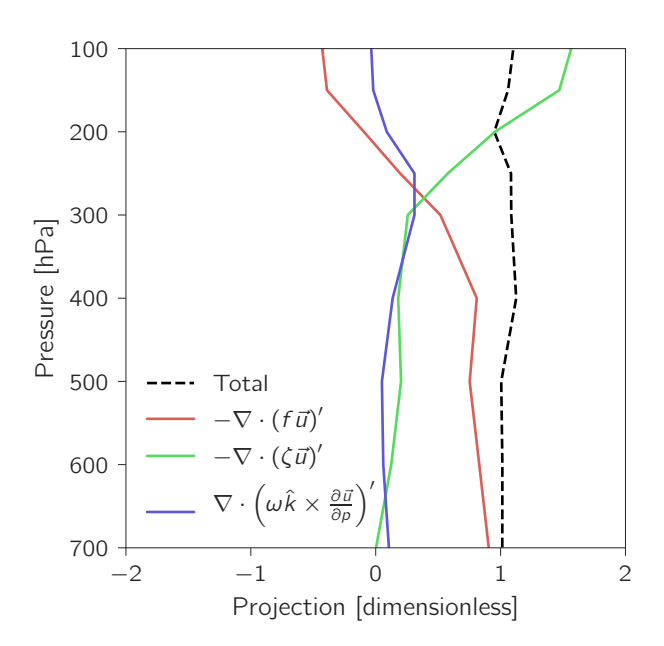


FIG. 10. Projection of vorticity budget terms on the time tendency of the relative vorticity.

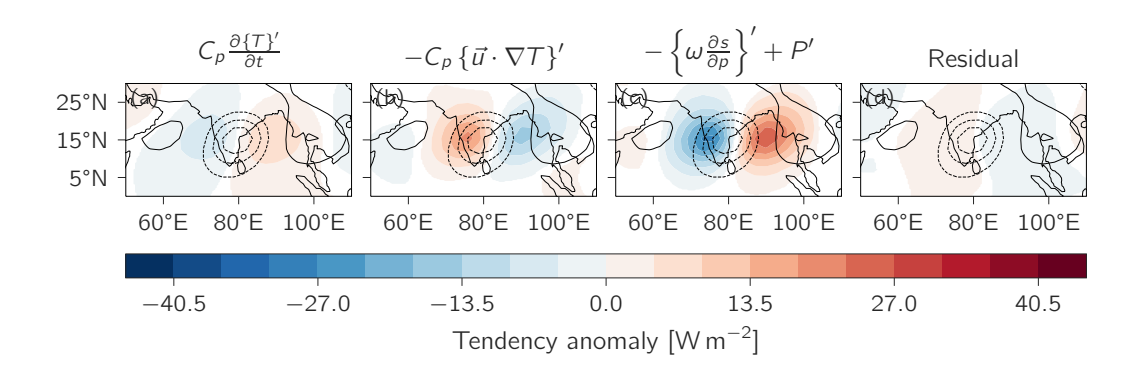


FIG. 11. Terms in the anomalous internal energy budget (colors) with anomalous column-integrated internal energy, $C_p\{T\}'$, overlaid (contours). Only budget values statistically significant at a 99% level are shown. Negative contours are dashed; positive contours are solid. With the exception of the omission of the zero contour, contours are separated by an interval of $2.5 \times 10^5 \, \mathrm{Jkg^{-1}}$.

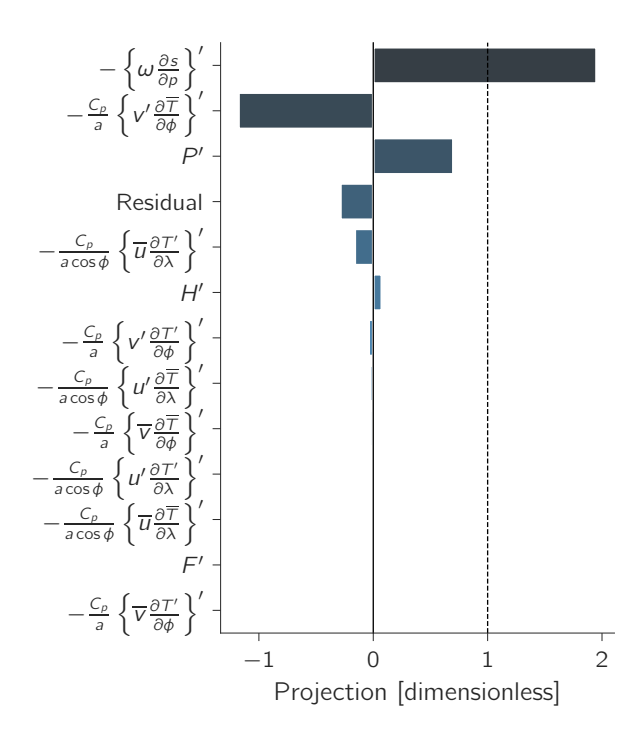


FIG. 12. Projection of the terms on the right hand side of the column-integrated internal energy budget sorted in descending order by absolute value. The horizontal advection term is comprehensively decomposed into linear and nonlinear components. The sum of the components adds exactly to 1.0.

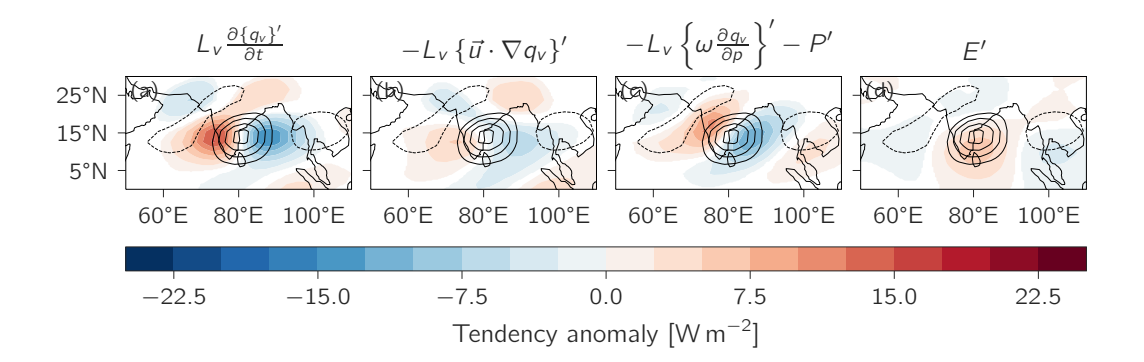


FIG. 13. Terms in the anomalous moisture budget (colors). Only tendency anomalies statistically significant at the 99% level are shown. Contours represent column-integrated moisture anomalies scaled by the latent heat of vaporization, L_{ν} . Negative contours are dashed; positive contours are solid. With the exception of the omission of the zero contour, contours are separated by intervals of $4.0 \times 10^5 \,\mathrm{J}\,\mathrm{m}^{-2}$.

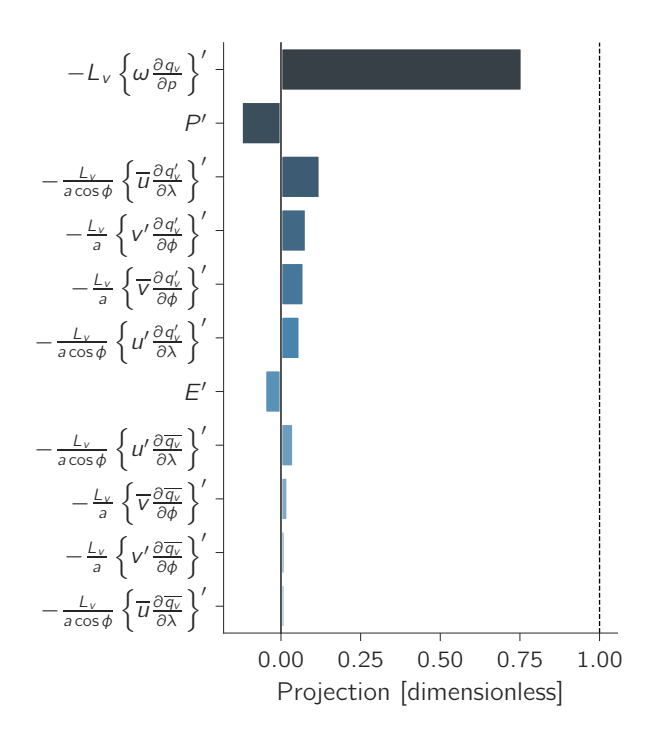


FIG. 14. Projection of the terms on the right hand side of the column-integrated moisture budget sorted in descending order by absolute value. The horizontal advection term is comprehensively decomposed into linear and nonlinear components. The sum of the components adds exactly to 1.0.